Markedly different impacts of primary emissions and secondary aerosol formations on aerosol mixing states revealed by simultaneous measurements of CCNC, V/HTDMA and SP2

Jiangchuan Tao[1,8], Biao Luo[1,8], Weiqi Xu[3], Gang Zhao[6], Hanbin Xu[5], Biao Xue[1,8], Miaomiao Zhai[1,8], Wanyun Xu[4], Huarong Zhao[7], Sanxue Ren[7], Guangsheng Zhou[7], Li Liu[2,*], Ye Kuang[1,8,*] , Yele Sun[3]

[1] Institute for Environmental and Climate Research, Jinan University, Guangzhou, Guangdong, China

[2] Key Laboratory of Regional Numerical Weather Prediction, Institute of Tropical and Marine Meteorology, China Meteorological Administration, Guangzhou, China.

[3] State Key Laboratory of Atmospheric Boundary Layer Physics and Atmospheric Chemistry, Institute of Atmospheric Physics, Chinese Academy of Sciences, Beijing, China.

[4] State Key Laboratory of Severe Weather, Key Laboratory for Atmospheric Chemistry, Institute of Atmospheric Composition, Chinese Academy of Meteorological Sciences, Beijing, China

[5] Experimental Teaching Center, Sun Yat-Sen University, Guangzhou, China

[6] State Key Joint Laboratory of Environmental Simulation and Pollution Control, International Joint Laboratory for Regional Pollution Control, Ministry of Education, College of Environmental Sciences and Engineering, Peking University, Beijing 100871, China

[7] Hebei Gucheng Agricultural Meteorology National Observation and Research Station, Chinese Academy of Meteorological Sciences, Beijing, 100081, China

[8] Guangdong-Hongkong-Macau Joint Laboratory of Collaborative Innovation for Environmental Quality, Jinan University, Guangzhou, Guangdong, China

Correspondence: Ye Kuang (kuangye@jnu.edu.cn), Li Liu (liul@gd121.cn)

Abstract

The aerosol mixing state is a crucial physical-chemical property that affects their optical properties and cloud condensation nuclei (CCN) activity. Multiple techniques are commonly employed to determine aerosol mixing states for various applications, and comparisons between these techniques provide insights of the variations in aerosol chemical and physical properties. These techniques include size-resolved CCN activity measurements using a system with CCN counter (CCNC) coupled with a differential mobility analyzer (DMA), a Humidified/Volatility Tandem differential mobility analyzer (H/V-TDMA) which measures aerosol hygroscopicity/volatility distributions, and a single particle soot photometer (SP2) which directly quantifies black carbon (BC) mixing states. This study provides a first time intercomparisons of aerosol mixing state parameters obtained through simultaneous measurements of a DMA-CCNC, a H/VTDMA and a DMA-SP2. The impact of primary aerosols emissions and secondary aerosol formations on the aerosol mixing states and intercomparison results were analyzed. The results showed that differences in mixing state parameters measured by different techniques varied greatly under different conditions. The V-TDMA and DMA-SP2 measurements showed that the non-volatile population identified by the V-TDMA was mainly contributed by BC-containing aerosols. The HTDMA and DMA-SP2 measurements indicated that a substantial proportion of nearly hydrophobic aerosols were not contributed from BC-containing aerosols, but likely originated from fossil fuel combustion and biomass burning emissions. Synthesized comparison results between DMA-CCNC, HTDMA and DMA-SP2 measurements revealed that some of the nearly hydrophobic BC-free particles were CCN-inactive under supersaturated conditions, likely from fossil combustion emissions, while others were CCN-active under supersaturated conditions linked to biomass burning emissions. Fossil fuel combustion-emitted BC-containing aerosols tended to be more externally mixed with other aerosol components compared to those emitted from biomass burning activities. These results highlight significant disparities in the mixing states as well as physiochemical properties between aerosol originated from fossil fuel combustion and biomass burning. The formation of secondary nitrate and organic aerosols exerted significant impacts on variations in aerosol mixing states, generally enhancing aerosol hygroscopicity and volatility, while reducing differences in mixing state parameters derived from different techniques, resulting in a reduction in aerosol heterogeneity. The variations in BC-free particle number fractions showed that secondary aerosols tended to form

more quickly on BC-free particles than on BC-containing particles. Further comparison of mixing state parameters revealed that the two resolved secondary organic aerosol factors in this study exhibited remarkably different physical properties, indicating that they were likely formed through different pathways. These findings suggest that intercomparisons among aerosol mixing states derived from different techniques can provide deeper insight into aerosol physical properties and how they are impacted by secondary aerosol formation, aiding the investigation of secondary aerosol formation pathways.

1 Introduction

The aerosol mixing state is a crucial physicochemical property of aerosol particles (Riemer et al., 2019), exerting a significant impact on their optical properties and cloud condensation nuclei (CCN) activity, affecting their impact on climate and the environment (Fierce et al., 2017; Riemer et al., 2019; Stevens et al., 2022). For instance, variations in the mixing state of black carbon (BC) particles can significantly alter their absorption and radiative effects (Bond et al., 2013; Lack et al., 2012; Zhao et al., 2019; Moffet et al., 2016; Matsui et al., 2018; Peng et al., 2016). Using simple internally mixing state assumptions for aerosol chemical compositions in estimating CCN number concentrations can lead to substantial overestimations (up to 30%, Deng et al., 2013; Farmer et al., 2015; Ren et al., 2018; Ching et al., 2017, 2019; Tao et al., 2021). The aerosol mixing state varies widely due to complex emissions and atmospheric transformations, leading to significant uncertainties in estimating the effects of aerosol based on simplified mixing state assumptions (Ervens, 2015; Wang et al., 2022; Fu et al., 2022).

The aerosol mixing state describes the mixture of aerosol chemical components within each single particle and the distribution of these particles in the aerosol population. This property can be directly measured by the single particle chemical composition techniques (Fierce et al., 2017; Riemer et al., 2019), such as single particle soot photometer (SP2) that measures refractory black carbon (rBC) mass concentrations and the mixing state of rBC with other aerosol components or single particle chemical composition measurement techniques (e.g. Single Particle Aerosol Mass Spectrometer, SP-AMS) that have been developed over recent years (Lee et al., 2019; Riemer et al., 2019 and reference therein). Alternatively, the aerosol mixing state can be inferred from indirect measurements of aerosol properties, such as size-resolved aerosol CCN activity (measured by coupling a differential mobility analyzer (DMA) and a CCN counter (CCNC)), size-resolved aerosol hygroscopicity distributions or volatility distributions (measured by a Humidified/Volatility Tandem differential mobility analyzer (H/V-TDMA)).

However, each technique yields information on aerosol mixing states based on different aerosol micro-physical properties, thus obtain aerosol mixing states that are different but linked to one another. For instance, while both CCN activity and the hygroscopic growth measurements are associated with aerosol hygroscopicity, intercomparison between CCNC and HTDMA measurements promoted

investigations on aerosol hygroscopicity variations under different saturation conditions (Su et al., 2010; Juranyi et al., 2013; Lance et al., 2013; Kawana et al., 2016; Tao et al., 2020; Jiang et al., 2021). Although both SP2 and VTDMA techniques depend on the evaporation of non-refractory compositions, only the rBC remains in SP2 measurements, whereas the non-refractory composition evaporations depend on thermodenuder temperature in VTDMA measurements. Thus, measurements of an SP2 are highly correlated to those of a VTDMA at high temperatures (higher than 200 °C and up to 300 °C), with their differences reflecting variations in aerosol density, shape or volatility (Philippin et al., 2004; Wehner et al., 2009; Adachi et al., 2018, 2019; Wang et al., 2022). HTDMA and VTDMA can be applied in combination to study the influence of aerosol mixing state on its hygroscopicity and volatility (Zhang et al., 2016; Cai et al., 2017; Wang et al., 2017). Strong correlations were found between hydrophobic and non-volatile particles, suggesting that they might be of similar chemical composition (Zhang et al., 2016). In addition, some studies showed that except for BC, low-volatility particles correlated well with CCN-inactive particles based on VTDMA and CCNC measurements (Kuwata et al., 2007; Kuwata and Kondo, 2008; Rose et al., 2011; Cheng et al., 2012). Therefore, intercomparisons between mixing state parameters measured by distinct techniques provides not only better characterization of the aerosol mixing state itself, but also insight into aerosol physiochemical properties. Previous studies have mainly compared two kinds of aerosol mixing state measurements, lacking comprehensive comparative analysis among SP2, DMA-CCN, and HV-TDMA measurements, hindering the wide applications of derived aerosol mixing states obtained by individual techniques.

The mixing state of primary aerosols can vary greatly depending on their type and emission conditions (Cheng et al. 2012; Wang et al. 2017; Wang et al., 2022; Ting et al., 2018; Liu et al., 2021), and can be significantly altered during aging processes or secondary formations (Wehner et al. 2009; Cheng et al. 2012; Wang et al., 2022; Tomlin et al., 2021; Lata et al., 2021). Primary aerosol emissions such as biomass burning, fossil fuel combustion and cooking tend to contribute to weakly hygroscopic (Herich et al., 2008, 2009; Wang et al., 2020; Kim et al., 2020) and low-volatility aerosols (Hong et al., 2017; Saha et al., 2018), while formation of secondary aerosol including aging of BC-containing aerosols and primary organic aerosols mainly contribute to aerosols with strong CCN activity (Mei et al., 2013; Ma et al., 2016; Tao et al., 2021) and high hygroscopicity (Chen et al., 2018; Kim et al., 2020; Wang et al., 2020). To enhance our understanding of the mixing state of aerosols from different

emission sources and to improve its characterization in models, it is important to study the impact of specific primary aerosol emissions and secondary aerosol formations on aerosol mixing states and the influence on aerosol mixing state parameters derived from different techniques.

The North China Plain (NCP) is among the most polluted regions in China with various primary emission sources and strong secondary aerosol formations playing critical roles in air pollution (Xu et al., 2011; Tao et al., 2012; Liu et al., 2015). The complex mixing state of aerosols in the NCP contributes to uncertainties in evaluating their climate and environmental effects (Zhuang et al., 2013; Nordmann et al., 2014; Zhang et al., 2016; Tao et al., 2020; Shi et al., 2022), particularly with regards to BC particles (Wu et al., 2017; Liu et al., 2019; Zhao et al., 2019; Wang et al., 2011; Zheng et al., 2019). Meteorological conditions can greatly impact the secondary aerosol formation in the NCP, which can be significantly exacerbated during severe pollution events. The secondary aerosol formations under low RH conditions, mainly taken place in gaseous phase, would change to that mainly taken place in aqueous phase under high RH conditions (Kuang et al., 2020). As secondary aerosols formed through different mechanisms have different chemical compositions and add mass to different particle groups, secondary aerosol formations under different meteorological conditions can affect the aerosol mixing states (Tao et al., 2021). This study obtained aerosol mixing state through concurrent measurements of CCN activity, hygroscopicity, volatility and BC particle at a regional site in the NCP, using CCNC, HTDMA, VTDMA and SP2 instruments. This provides a unique opportunity to perform a most comprehensive intercomparison of aerosol mixing state among different techniques for insights into the impact of primary aerosol emissions and secondary aerosol formations on the observed aerosol mixing states.

2 Materials and methods

2.1 Campaign information and instruments set-up

From 16th October to 16th November 2021, aerosol mixing states were continuously and concurrently monitored using different techniques at the Gucheng site in Dingxing county, Hebei province, China, as part of the campaign of investigating AQueous Secondary aerOsol formations in Fogs and Aerosols and their Radiative effects in the NCP (AQ-SOFAR). The observation site, located at 39°09’N, 115°44’E, is an Ecological and Agricultural Meteorology Station of the Chinese Academy

of Meteorological Sciences, situated between the megacities of Beijing (approximately 100 km away) and Baoding (approximately 40 km away), and surrounded by farmlands and small towns. This site provides a representative view of the background conditions of atmospheric pollution in the NCP (Kuang et al., 2020; Li et al., 2021).

Different measurement techniques were used during the campaign to simultaneously obtain the aerosol mixing state through CCN activity, hygroscopicity, volatility, and BC particle observations (to be discussed in the next section). In addition to aerosol mixing state measurements, the AQ-SOFAR campaign also included measurements of aerosol number size distribution, chemical composition, aerosol scattering and absorption properties. The aerosol number size distribution covered diameter range of 13 nm to 4 μm are measured by the scanning mobility particle sizer (13-550 nm) and the aerodynamic aerosol classifier (100 to 4 μm), and they are merged together by assuming the aerosol density of 1.6 g/cm^3. The total BC mass concentrations were determined using an aethalometer (Magee, AE33; Drinovec et al., 2015), with more information about the correction of the absorption measurements and mass concentration calculations available in Luo et al. (2022). All aerosol measurement instruments were housed in a temperature-controlled container set at 24 °C. The inlet was switched among three impactors: TSP (Total Suspended Particles), $PM_{2.5}$ (Particulate matter with aerodynamic diameter less than 2.5 μm) and PM_1 (Particulate matter with aerodynamic diameter less than 1 μm). Inlet changes would affect the dry state aerosol sampling due to aerosol hygroscopic growth or activation. However, the aerosol mixing state and aerosol chemical composition measurements were made on submicron aerosols, inlet change almost does not affect those measurements under conditions of RH less than 90%, and this would be discussed very carefully in our next paper. The sampled aerosol was dried by two parallelly assembled Nafion dryers with length of 1.2 m. During autumn and winter in the NCP, ambient air temperature (lower than 20 °C and can down to 0 °C) can be significantly lower than the room temperature (~24 °C), this dryer can maintain the RH of sampled aerosols to below 20%. Meteorological data, such as temperature, pressure, wind speed and direction, relative humidity (RH), were obtained from an automatic weather station operated by the station.

The chemical composition of submicron aerosols was analyzed using a High-Resolution Time-of-Flight Aerosol Mass Spectrometer (HR-ToF-AMS). The ionization efficiency (IE) was calibrated using 300 nm diameter pure NH_4NO_3 particles, following the standard protocols outlined in Jayne et

al. (2000) in the middle of the campaign, with the relative ionization efficiency (RIE) of ammonium determined to be 5.26. The RIE of sulfate was 1.28 using pure $(NH_4)_2SO_4$ particles, and the default RIEs of 1.4 for organic aerosols, 1.1 for nitrates, and 1.3 for chlorides were used. The composition dependent collection efficiency reported by Middlebrook et al. (2012) was used in this study. Elemental ratios were derived using the "Improved-Ambient (I-A)" method as described in Canagaratna et al. (2015), including hydrogen to carbon (H/C), oxygen to carbon (O/C), and organic mass to organic carbon (OM/OC) ratios. Two POA (Primary Organic Aerosol) factors and two oxygenated organic aerosol (OOA) factors were identified by HR-PMF (High-Resolution Positive Matrix Factorization, Ulbrich et al., 2009; Paatero and Tapper, 1994). Summations of the two OOA factors are used to represent secondary organic aerosols (SOA) in this study. The mass spectra of the OA factors and their correlations with external species are shown in Figs. S1-S2. The BBOA (Biomass Burning Organic Aerosol) spectrum was characterized by obvious *m*/*z* 60 (mainly $C_2H_4O_2^+$) and 73 (mainly $C_3H_5O_2^+$), two indicators of biomass burning (Mohr et al., 2009). In addition, BBOA was correlated well with $C_2H_4O_2^+$ (R^2=0.91) and $C_3H_5O_2^+$ (R^2=0.90). Consistent with previous studies in Beijing (Xu et al., 2019), the PMF analysis revealed a mixed factor named FFOA (Fossil Fuel Organic Aerosol) that comprises traffic emissions and coal combustions, which was characterized by typical hydrocarbon ion series. It was observed that FFOA had a relatively high f_{44} (0.083) value, which is likely due to aging during regional transportation, similar to the results observed in the winter of 2016 in Beijing (Xu et al., 2019) and coal combustion organic aerosol in Gucheng (Chen et al., 2022). Secondary organic aerosol formations originated from volatile organic compounds precursors could be formed in differ formation pathways such as aqueous phase reactions, heterogeneous reactions or gas phase reactions and also might be oxidized under different conditions, for example, oxidized under different nitrogen oxide conditions with different oxidation capacity and oxidants. Two resolved OOA factors were found to display different spectral patterns, correlations with tracers and diurnal variations, suggesting that they resulted from different chemical processing, however, their formation mechanisms remain to be explored in our future studies. In general, the OOA factor 1 (OOA1) had higher CO2+/C2H3O+ (3.9) and O/C (0.91) ratios compared to the OOA factor 2 (OOA2, 2.1 and 0.78).

Note that losses in inlet line and sampling systems are not considered in this study. reasons are listed below: (1) investigated mixing state parameters are represented by number fractions of different diameters which are much less affected by losses in sampling systems compared with absolute umber concentrations; (2) good consistency was achieved between measurements of particle number size distributions (PNSD) by and mass concentrations measured by AMS, with the average ratio between volume concentration derived from AMS and rBC measurements and volume concentration derived from PNSD measurements is 0.79 (R=0.97, as shown in Fig. S3), which is consistent with previous reports due to that AMS cannot detect aerosol components such as dust (Kuang et al., 2021). This means that almost same aerosol populations were sampled by AMS and instruments of measuring aerosol mixing states.

2.2 Aerosol mixing states measurement techniques

2.2.1 DMA-CCNC measurements

The CCN activity of particles under supersaturated conditions was measured using a DMA-CCNC system, which consisted of a differential mobility analyzer (DMA, model 3081 by TSI, Inc., MN USA), a condensation particle counter (CPC, model 3756 by TSI, Inc., MN USA), and a continuous-flow CCNC (model CCN100 by Droplet Measurement Technologies, USA). The system operated in a size-scanning mode and provided the Size-resolved Particle Activation Ratio (SPAR) by combining the CPC and CCNC measurements at different particle sizes. In order to perform intercomparisons among instruments, three supersaturations (SSs) of 0.08%, 0.14% and 0.22% were applied in a single cycle of about 15 minutes. CCN measurement under these three SSs reveals mainly CCN activity of aerosols reside in accumulation mode aerosol with diameter range of about 100-200 nm, which are close to diameters of HV-TDMA measurements, and higher SSs would reveal CCN activity of smaller aerosol particles (<100 nm) where DMA-SP2 measurement is not available. The sample and sheath flow rates of the DMA were set at 1 lpm and 5 lpm, respectively, resulting in a measured particle diameter range of 9 nm to 500 nm with a running time of 5 minutes per cycle. Supersaturations in the CCNC were calibrated with monodisperse ammonium sulfate particles (Rose et al., 2008) both before and after the campaign. The flow rates were also calibrated before and after the campaign and were checked daily to minimize uncertainties in the droplet counting and supersaturation formed in the column (Roberts and Nenes, 2005; Lance et al., 2006). The SPAR

deviations due to multiple-charge particles were corrected using a modified algorithm based on Hagen and Alofs (1983) and Deng et al. (2011). More details about the system can be found in Ma et al. (2016) and Tao et al. (2021).

2.2.2 H/V-TDMA measurements

The mixing state of aerosols in terms of hygroscopicity and volatility was measured using a Hygroscopicity/Volatility Tandem Differential Mobility Analyzer (H/V-TDMA; Tan et al., 2013). The H/V-TDMA consists of two DMA (Model 3081L, TSI Inc.), with the first DMA (DMA1) selecting dried particles without conditioning and the second DMA (DMA2) selecting conditioned particles. The H/V-TDMA can operate in either H-mode or V-mode, which is controlled by a three-way solenoid valve. In H-mode, a Nafion humidifier is used to condition the selected dry particles to 90% relative humidity (RH) equilibrium. The number size distribution of the humidified particles (Dp) is measured by DMA2 and a CPC (Model 3772, TSI Inc.). The RH-dependent hygroscopic growth factor (GF) at a certain dry diameter (D_d) is calculated as follows:

$$GF=\frac{D_p(RH)}{D_d} \quad (1)$$

Where Dp(RH) is the particle diameter undergo humidification. In this mode, four dry electrical mobility diameters (50, 100, 150 and 200 nm) were measured. The instrument was regularly calibrated using Standard Polystyrene Latex Spheres (PSL) and Ammonium Sulfate particles.

In the V-mode, a heated tube was used to evaporate the volatile coatings from the previously selected dry particles. Six temperature settings were used for the heated tube, ranging from 25 to 200°C. The number size distributions of the heated particles were measured using DMA2 and CPC. Besides the four particle sizes measured in H-mode, three additional particle sizes (250, 300 and 350 nm) were measured in the V mode. The temperature dependent shrinkage factor (SF), which is the ratio of the heated particle size to the dry particle size without heating (D_d), is defined as:

$$SF=\frac{D_p(T)}{D_d} \quad (2)$$

Where Dp(T) is the particle diameter undergo heating. A complete cycle of both H-mode measurements at one relative humidity (RH) condition and V-mode measurements at six temperature conditions took approximately 3 hours. A Probability Density Function (PDF) of GF (or SF) can be

calculated from the measured density function using the inversion algorithm described by Stolzenburg and McMurry (2008).

2.2.3 DMA-SP2 measurements

The size-resolved BC mixing states were measured by the SP2 (Droplet Measurement Technology, Inc., USA) after a DMA (Model 3081, TSI, USA). The DMA selected aerosols at various dry particle sizes, which were then introduced to the SP2. The DMA-SP2 setup was able to measure the mixing states of aerosols at diameters of 100 nm, 120 nm, 160 nm, 200 nm, 235 nm, 270 nm, 300 nm, 335 nm, 370 nm, 400 nm, 435 nm, 470 nm, 500 nm, 535 nm, 570 nm, 600 nm, 635 nm, 670 nm, 700 nm within 20 minutes, when it wasn't placed after a thermodenuder-bypass switch system (13^{th}-24^{th} October, 09:00 am of 5^{th} November to 09:00 am of 8^{th} November). However, it only measured mixing states at diameters of 120 nm, 160 nm, 200 nm, 250 nm, 300 nm, 400 nm, and 500 nm when it was placed after a thermodenuder-bypass switch system (11:00 am 24^{th} October to 08:00 am 5^{th} November, and 09:00 am of 8^{th} November to 06:00 pm of 17^{th} November). Because the measurements of HTDMA and VTDMA are conducted solely by a single H/VTDMA system working in different mode, the time needed for a single particle size measurement of HTDMA and VTDMA is much longer than that of DMA-SP2 system. Thus, more particle sizes are selected in the measurement DMA-SP2 system for acquiring BC mass concentration and mixing state at more diameters, compared to those of HTDMA and VTDMA.

The SP2 chamber has a continuous Nd: YAG laser beam at a wavelength of 1064 nm. The BC-containing particles passing through the laser beam will be incandescent through absorbing the radiation. By measuring the intensity of the emitted incandescent light, the mass concentration of BC can be calculated. The sheath flow/sample flow ratio was maintained at 10 for DMA to reduce the width of diameter distribution of selected monodisperse aerosols. Additionally, the flow rate of the SP2 was changed from 0.1 to 0.12 L/min starting on October 22nd (flow rate range of SP2: 0.03 to 0.18 L/min). The SP2 was calibrated using Aquadag soot particles, as reported by Gysel et al. (2011). Further details about the calibrations are introduced in Section 1 of the supplement.

2.3 Derivations of mixing state parameters

2.3.1 Fitting SPAR curves measured by the DMA-CCNC system

The measured SPAR curves can be parameterized with a sigmoidal function with three parameters. As shown in Fig. S4, the measured SPAR is generally characterized as a sigmoidal curve. This parameterization assumes that the aerosol is an external mixture of hydrophilic particles that are CCN-active and hydrophobic particles that are CCN-inactive (Rose et al., 2010). The formula used to parameterize SPAR ($R_a(D_d)$) for a specific SS is as follows (Rose et al., 2008):

$$R_a(D_d)=\frac{MAF}{2}\left(1+erf\left(\frac{D_d-D_a}{\sqrt{2}\sigma}\right)\right) \quad (7)$$

where erf is the error function. MAF (Maximum Activation Fraction) is an asymptote of the measured SPAR curve at large particle sizes as shown in Fig. S4, and it represents the number fraction of CCNs to total particles. D_a is the midpoint activation diameter and is linked to the hygroscopicity of CCNs, and indicates the diameter where SPAR equals the half of the MAF value. σ is the standard deviation of the cumulative Gaussian distribution function and characterizes the heterogeneity of CCN hygroscopicity. In Fig. S4, the parameter corresponds to the slope of steep increase of SPAR curves when diameter is close to Da. Generally, hydrophilic particles larger than D_a can become CCN, so these three parameters can be used to characterize the hygroscopicity of those hydrophilic particles. This study did not consider the impact of nearly hydrophobic particles on SPAR, as deviations from this parameterization scheme due to this impact are negligible at low SSs, as stated in Tao et al. (2020).

2.3.2 Classification of particle type based on hygroscopicity or volatility

In this study, ambient aerosol particles were classified into two groups based on their hygroscopicity (hydrophobic and hydrophilic) and two groups based on their volatility (non-volatile and volatile) based on the measurements from H/V-TDMA (Wehner et al., 2009; Liu et al., 2011; Zhang et al., 2016). Each group can be defined using a critical value of GF or SF as the following:

Hydrophobic population: $GF < GF_C$;

Hydrophilic population: $GF \geq GF_C$;

Non-volatile population: $SF \geq SF_C$;

Volatile population: $SF < SF_C$.

The critical values of GF (GF_C) and SF (SF_C) in H/V-TDMA depend on particle size and working conditions such as relative humidity and heating temperature.

During this campaign, the SF_C was set at 0.85 for all seven measured particle sizes at a temperature of 200 °C. The GF_C for the four measured particle sizes of 50 nm, 100 nm, 150 nm and 200 nm were 1.1, 1.15, 1.175 and 1.2, respectively, and the corresponding hygroscopicity parameter, κ, was approximately 0.07. These values of GF_C and SF_C divide the probability density functions (PDFs) of SF and GF into two modes, consistent with prior studies in the NCP (Liu et al., 2011; Zhang et al., 2016). The number fraction (NF) for the hydrophilic group (NF_H) and volatile group (NF_V) can be calculated as:

$$NF_H = \int_{GF_C}^{\infty} GFPDF(GF)dGF \quad (7)$$

$$NF_V = \int_{0}^{SF_C} SFPDF(SF)dSF \quad (8)$$

where GFPDF and SFPDF are the PDFs of GF and SF, respectively, derived from H/V-TDMA measurements.

2.3.3 Classification of particle type based on DMA-SP2 measurements

The BC-containing aerosols can be categorized into two groups based on the coating thickness: bare BC/thinly coated BC particles and thickly coated BC particles. For measurement of coated BC particles in SP2, the incandescence signals is generally detected later than the scattering signals and the time difference between the occurrences of the peaks of the incandescence and scattering signals is defined as the lag time (Moteki & Kondo, 2007; Sedlacek et al., 2012; Subramanian et al., 2010). The coating thickness of the BC-containing aerosols in the SP2 measurement can be indicated by the lag time between the peak of the scattering signal and the incandescence signal (Moteki and Kondo, 2007; Schwarz et al., 2006; Sedlacek et al., 2012; Subramanian et al., 2010; Metcalf et al., 2012), which exhibits a clear two-mode distribution in former studies (Zhang et al., 2018; Zhao et al., 2021). A critical lag time threshold can be used to differentiate between the different types of BC-containing aerosols and calculate the number fraction of bare BC particles and coated BC particles in the total identified aerosols. In this study, a two-mode distribution of the lag time (Δt) was observed. As the lag time is positively correlated to the coating thickness, a critical value of 0.8 μs was used to classify the

BC-containing particles into thinly coated (or bare) BC ($\Delta t < 0.8$ μs) and thickly coated BC ($\Delta t \geqslant 0.8$ μs), respectively. In addition, the definitions of all abbreviations are listed in Table 1.

Table 1. Definition and description of the abbreviations.

Abbreviations	Full name and/or Definition
BBOA	Biomass Burning Organic Aerosol In this study, characterized by obvious m/z 60 (mainly $C_2H_4O_2^+$) and 73 (mainly $C_3H_5O_2^+$), which are two indicators of biomass burning
FFOA	Fossil Fuel Organic Aerosol A mixed factor in this study that comprises traffic emissions and coal combustions, which was characterized by typical hydrocarbon ion series
OOA	Oxygenated Organic Aerosol
OOA1 and OOA2	Two OOA factors resolved from the PMF analysis
SOA	Secondary Organic Aerosol Summation of OOA1 and OOA2
POA	Primary Organic Aerosol Summation of BBOA and FFOA
$PM_{2.5}$	Particulate Matter with aerodynamic diameter less than 2.5 μm
PM_1	Particulate Matter with aerodynamic diameter less than 1 μm
NR-PM_1	Non-refractory PM_1
MF	Mass Fraction
Dp	Particle diameter after humidification or heating
Dd	Particle diameter under dry conditions without humidification or heating
κ	Hygroscopicity parameter
SS	Super-saturation

SPAR	Size-resolved Particle Activation Ratio Size-dependent CCN activity under a specific SS
MAF	Maximum Activation Fraction An asymptote of the measured SPAR curve at large particle sizes and represents the number fraction of CCNs to total particles
Da	Midpoint activation diameter Linked to the hygroscopicity of CCNs
GF	Growth factor The ratio between particle with and without humidification, and is linked to aerosol hygroscopicity
SF	Shrinkage Factor The ratio between particle with and without heating, and is linked to aerosol volatility
PDF	Probability Distribution Function
NF_H	Number Fraction of Hydrophilic aerosol whose hygroscopicity parameter is higher than ~0.07.
NF_V	Number Fraction of Volatile aerosol whose Shrink Factor at 200 °C is lower than 0.85.
NF_{noBC}	Number Fraction of BC-free particles
NF_{CBC}	Number Fraction of thickly coated BC particles
R_{exBC}	Number concentration ratio of externally BC particles in total BC-containing particles. Externally BC particles are defined as identified bare/thinly coated BC-containing particles
NF_A-NF_B (NF_{noBC}-NF_H, NF_V-NF_H, NF_{noBC}-NF_V, NF_V-MAF, NF_{noBC}-MAF)	The difference between the number fraction of A and B.

348

3 Results and discussions

3.1 Campaign Overview

The time series of meteorological parameters, aerosol mixing state measurements by different techniques and mass concentrations of aerosol chemical compositions are shown in Fig. 1. In detail, the measurements of aerosol mixing states include SPAR (Size-resolved Particle Activation Ratio) at SS of 0.08% by DMA-CCNC, GF-PDF (PDF of Growth Factor) at 200 nm by HTDMA, SF-PDF (PDF of Shrink Factor) at 200 nm and 200 °C by VTDMA, lag time PDF of 200 nm BC-containing particles

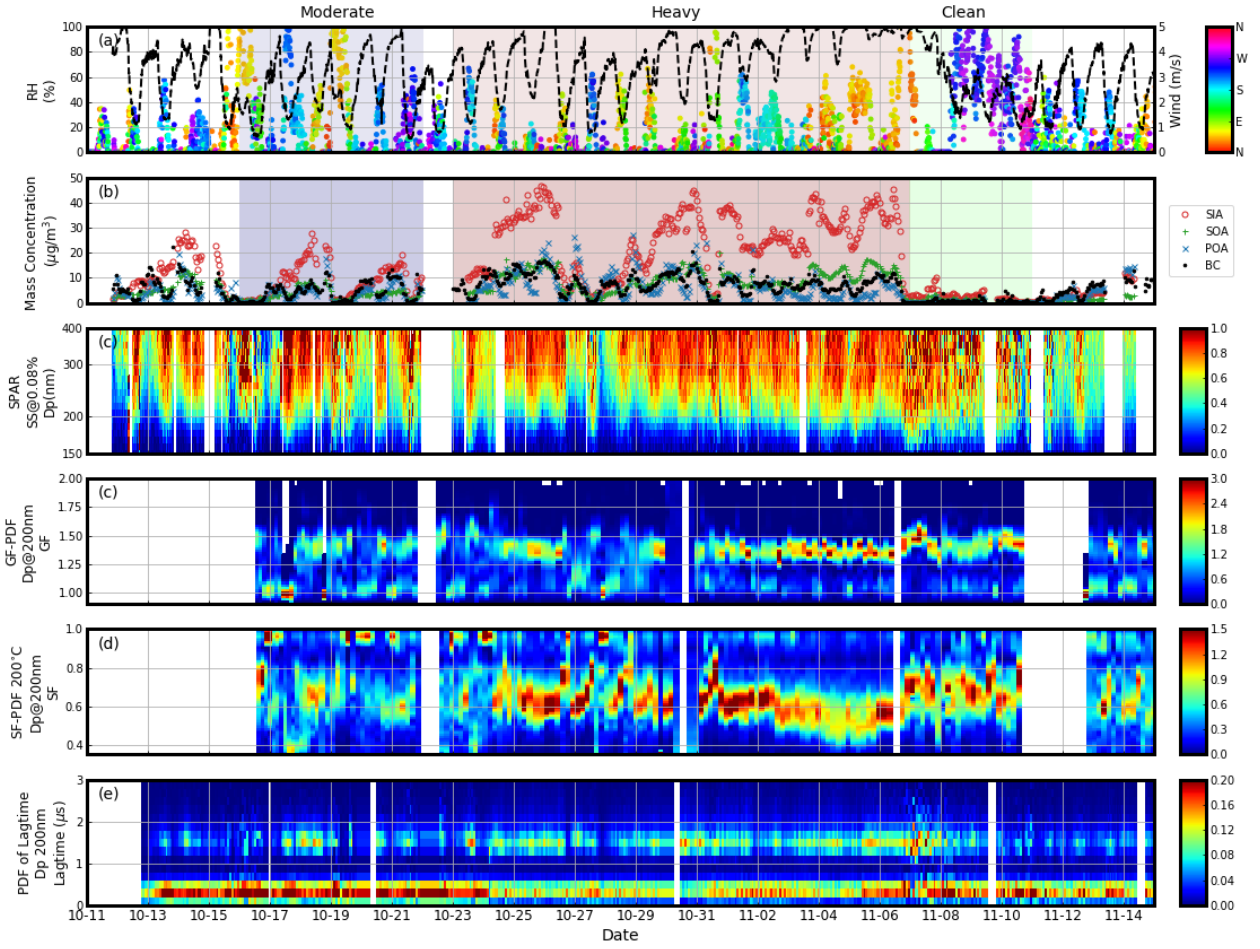

Figure 1. Overview of the measurements during the campaign: **(a)** meteorological parameters: wind speed (dots) and RH (black line), with colors of dots representing wind direction; **(b)** mass concentrations of aerosol chemical compositions: secondary inorganic aerosols (SIA, red circle), secondary organic aerosols (SOA, green plus), primary organic aerosols (POA, blue x) and black carbon (BC, black dots); **(c)** Size-resolved Particle Activation Ratio (SPAR) under supersaturation (SS) of 0.08% observed by DMA-CCN, with warmer colors corresponding to higher value; **(d)** PDF of growth factor (GFPDF) at 200 nm observed by HTDMA; **(e)** PDF of shrinkage factor (SFPDF) at 200 nm and 200 °C observed by VTDMA; **(f)** PDF of lag time at 200 nm observed by DMA-SP2. The blue, red and green shaded periods represent the three periods with moderate pollution, heavy pollution and clean condition, respectively.

by DMA-SP2. The mass concentrations of SIA (Secondary Inorganic Aerosols, include nitrate, sulfate and ammonium), SOA (Secondary Organic Aerosols, include two Oxygenated Organic Aerosol factors: OOA1+OOA2, POA (Primary Organic Aerosol, include Biomass Burning Organic Aerosol and Fossil Fuel Organic Aerosol) and BC are shown. During the campaign, three periods with significantly different aerosol pollution conditions were identified. As shown in Fig. 1(b), before October 23rd (moderately polluted period), the accumulation of aerosols led to SIA mass concentrations greater than 20 μg/m^3, while the highest concentrations of SOA, POA and BC mass all reached 10 μg/m^3. The mass concentrations of different aerosol components increased significantly from October 23rd to November 6th (heavily polluted period with average non-refractory PM_1 mass concentration of 49.5±22.5 μg/m^3) and decreased to much lower levels after November 6th(clean period with non-refractory PM_1 mass concentration of 5.1±3.3 μg/m^3).. Two particle groups were identified with regard to CCN activity, hygroscopicity, volatility and coating thickness, as demonstrated by SPAR, GF-PDF, SF-PDF, and the lag time PDF of BC-containing particles. Significant variations in aerosol mixing states were also observed during the three periods of different pollution conditions, as demonstrated by the variations in SF-PDF measured by the VTDMA. For example, the SF of the non-volatile particle group decreased during the heavily polluted period. Aerosol mixing states may have changed due to various transformations of existing aerosol particles and distinct secondary formation processes under different pollution conditions (Kuang et al., 2020; Tao et al., 2021; Shi et al., 2022; Yang et al., 2022). This will be analyzed in detail later in the discussion. The diurnal variations in mass concentrations of different aerosol chemical components and mixing states can be seen in the variations of SPAR measurements, as previously observed in this region (Liu et al., 2011; Ma et al., 2012; Kuang et al., 2015; Tao et al., 2020).

In Fig. 2, the campaign averaged SPAR at the three SSs, PDF of lag time of BC containing particles, GFPDF and SFPDF at 200 °C at different particle sizes are presented. The sigmoidal SPAR curves were characterized by a rapid increase followed by a gradual increase to unit 1, similar to measured SPAR curves previously observed in this region (Deng et al., 2011; Zhang et al., 2014; Ma et al., 2016; Tao et al., 2018). At lower SSs, the rapid increases in SPAR curves occur at larger particle sizes, since particle size need for CCN activation is larger. In addition, as SPAR in particle size lower than 300 nm is presented, the maximum AR of SPAR curves becomes smaller as there was less particle

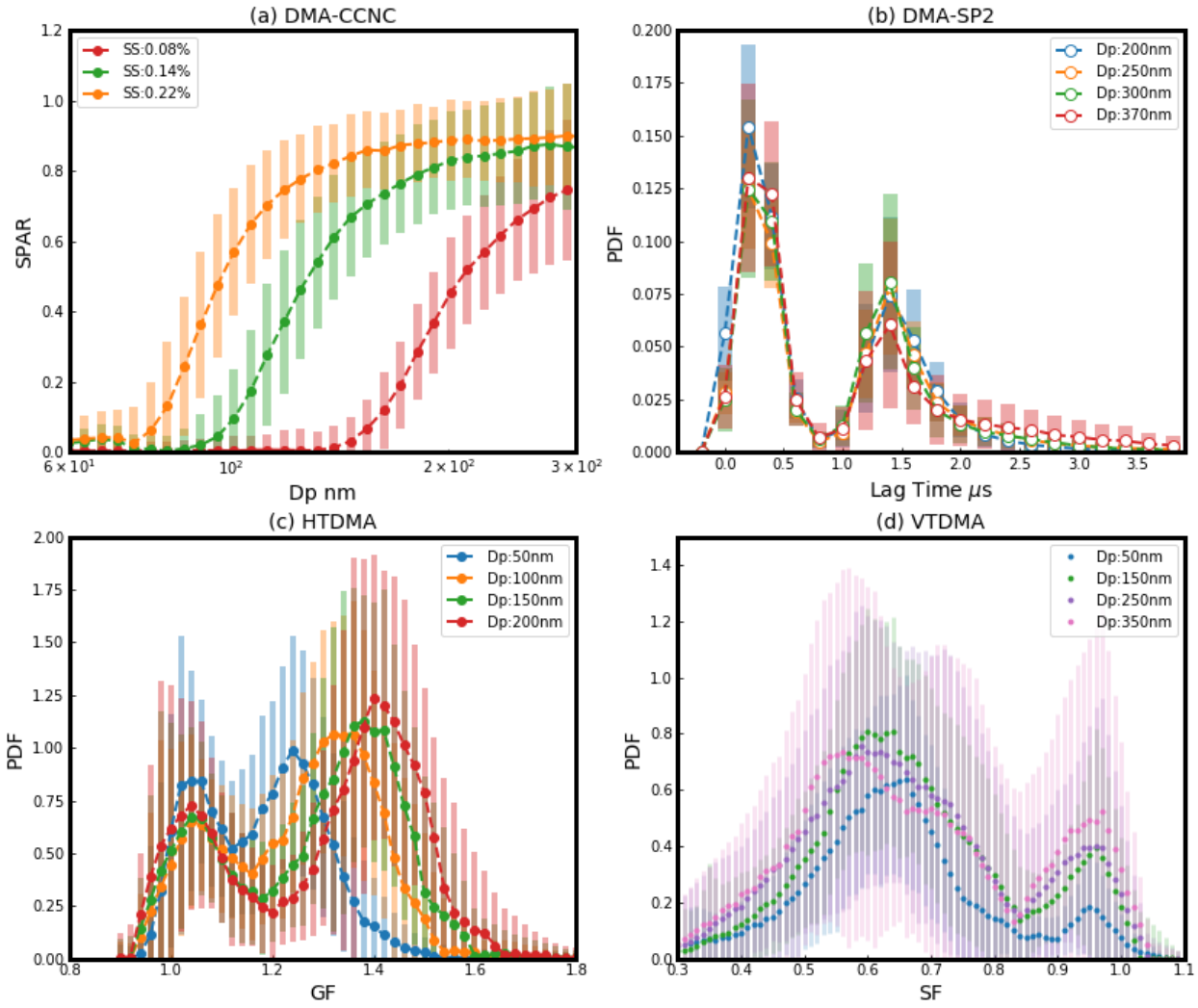

Figure 2. The campaign average of **(a)** Size-resolved Particle Activation Ratio (SPAR) curves measured by DMA-CCNC at the three supersaturations (SSs, represented by different colors and markers), **(b)** PDF of lag time measured by DMA-SP2 at four particle sizes (represented by different colors and markers), **(c)** PDF of growth factor GF (GFPDF) measured by HTDMA at four particle sizes(represented by different colors and markers), **(d)** PDF of shrinkage factor SF (SFPDF) measured by VTDMA under the temperature of 200 °C at five particle sizes(represented by different colors and markers). The shaded areas indicate the standard deviations.

to be CCN active under low SSs. For the three measured SSs, the particle size where SPAR equals about 0.5 are approximately 90 nm, 120 nm and 180 nm for the three SSs of 0.08%, 0.14% and 0.22%, respectively. These particle size agree with the value of the fitting parameter Da (midpoint activation diameter, see Eq.7) during the campaign, as the fitting parameter MAF (Maximum Activation Fraction, an asymptote of the measured SPAR curve at large particle sizes) is close to 1. The number fraction of CCN-active particles in large diameters range (which varies with SS and, for example, is greater than 200 nm for 0.08%) can be indicated by the gradual increase of SPAR curves and quantified by the

fitting parameter, MAF. The PDFs of the lag time, GF, and SF are all characterized by a bimodal distribution, which indicates two particle groups of BC-containing aerosols with different coating thicknesses, hygroscopicity and volatility. The variations in aerosol mixing states will be further analyzed on the basis of measured mixing state parameters.

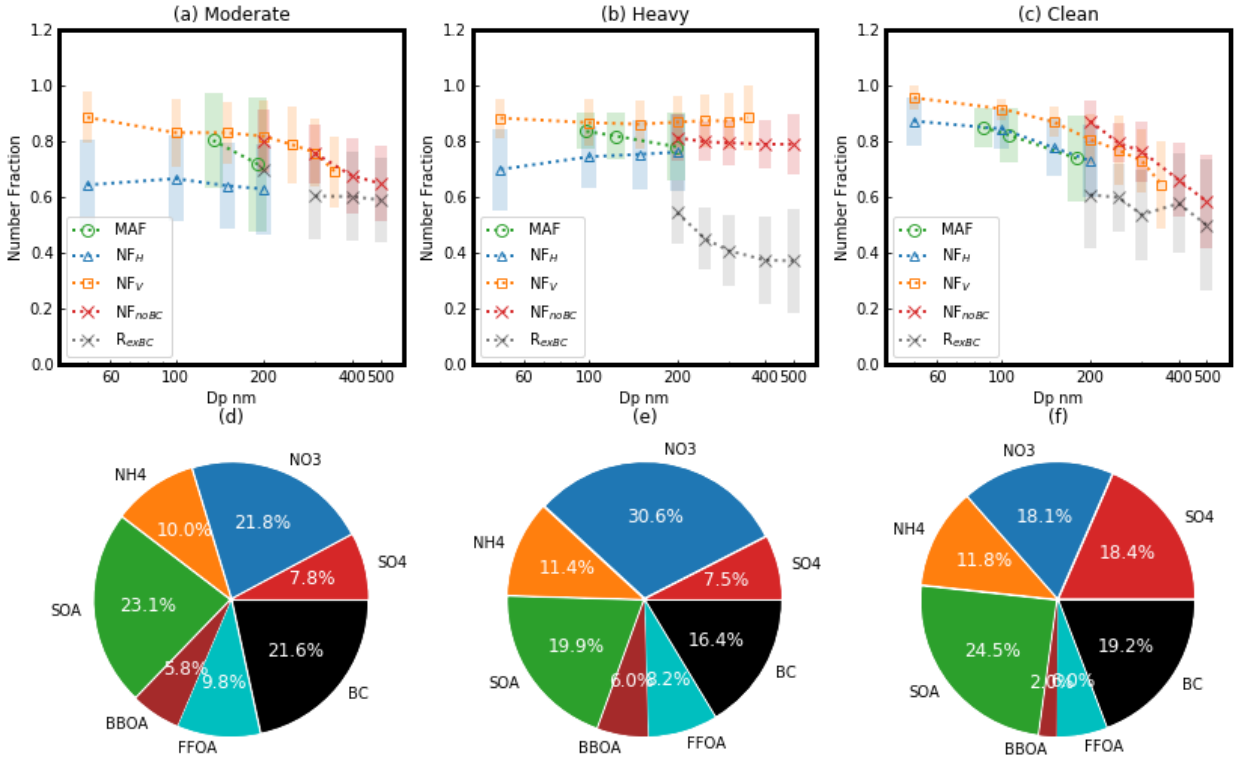

Figure 3. **(a-c):** Size dependence of MAF (green circle), NF_H (blue triangle), NF_V (yellow square), NF_{noBC} (red x) and R_{exBC} (black plus) during the three periods, **MAF** (Maximum Activation Fraction): An asymptote of the measured SPAR curve at large particle. **NF_H**: Number Fraction of Hydrophilic aerosol whose hygroscopicity parameter is higher than ~0.07. **NF_V**: Number Fraction of Volatile aerosol whose Shrink Factor at 200 °C is lower than 0.85. **NF_{noBC}**: Number Fraction of BC-free particles. **R_{exBC}**: Number fraction of externally BC particles in total BC-containing particles. **(d-f)**: Corresponding mass fractions of aerosol chemical compositions (identified by colors) during the three periods, including secondary organic aerosols (SOA), biomass burning organic aerosol (BBOA), fossil fuel organic aerosols (FFOA), and inorganic ions including sulfate (SO4), nitrate (NO3) and ammonium (NH4).

3.2 Intercomparisons among aerosol mixing state parameters derived using four techniques

The size dependence of aerosol mixing state parameters derived from measurements of the four techniques as well as the mass fraction of different aerosol chemical compositions during the three pollution periods are shown in Fig 3. In general, the size dependence of MAF, NF_H, NF_V and NF_{noBC}

were similar to one another, suggesting they were likely dominated by the same particle group, namely BC-free particles. This particle group had the highest fraction (higher than 0.7) during the heavily polluted period and the lowest fraction (down to 0.5) during the clean period, with the fraction decreasing with particle size. This suggests that primary emissions tend to have higher fractions of BC-containing particles in larger diameter ranges, for example, the fraction of BC-containing particles increases from ~0.1 to ~0.4 as particle size enlarges from 200 nm to 500 nm during the clean period. Since the bulk aerosol mass fraction (MF) is mostly contributed by particles larger than 300 nm, there might have been more hydrophilic, volatile, CCN-active and BC-free particles in larger sizes (> 300 nm) during the heavily polluted period, due to strong secondary aerosol formation in larger diameter ranges (Kuang et al., 2020), resulting in higher number fraction of these particles compared to the clean period. As for R_{exBC}, the small size dependence of R_{exBC} during the moderately polluted period might have been associated with stronger primary emissions, while the decrease of R_{exBC} with increasing particle diameter size in the polluted period confirms secondary aerosol formation to be more efficient on particles with larger diameter.

As for the difference among the aerosol mixing state parameters, NF_V and NF_{noBC} agreed with each other with a difference smaller than 0.1, and both were higher by at least 0.1 than NF_H in the moderately polluted period. In detail, compared to NF_{noBC}, NF_V was higher during the heavily polluted period, when the nitrate fraction was the highest (~30%) and the SOA fraction was the lowest (~7%) among all three periods, suggesting some BC-containing aerosols in this period were also identified as volatile, which is consistent with the fact that formation of semi-volatile nitrate in the BC-containing particles increases their volatility. However, during the clean period, NF_V was even lower than NF_{noBC}, suggesting that some BC-free aerosols were characterized as low volatile and non-negligible fractions of BC-free aerosols dominated these less volatile aerosol components, which were likely less volatile organic aerosols. In addition, the MAF values generally agreed with NF_H during the clean period, but were larger than NF_H during the moderately and heavily polluted periods (by ~0.2) when the POA/SOA fractions were higher (~40% vs ~35%). POA generally had lower hygroscopicity than SOA. The critical κ of hydrophilic mode aerosols was 0.07, suggesting that a higher fraction of aerosols had κ below 0.07 (i.e. hydrophobic mode aerosol in this study) during the moderately polluted period. However, under supersaturated conditions, they demonstrated enhanced hygroscopicity by becoming

CCN-active. The NF_H was consistently lower than NF_V and NF_{noBC} (the average difference between NF_H and NF_{noBC} was about 0.2). As mentioned above that NF_H was also lower than MAF during the moderately polluted periods, there may be a significant fraction of volatile BC-free aerosols had hygroscopicity lower than critical κ of 0.07 but were still CCN-active and therefore not fully hydrophobic.

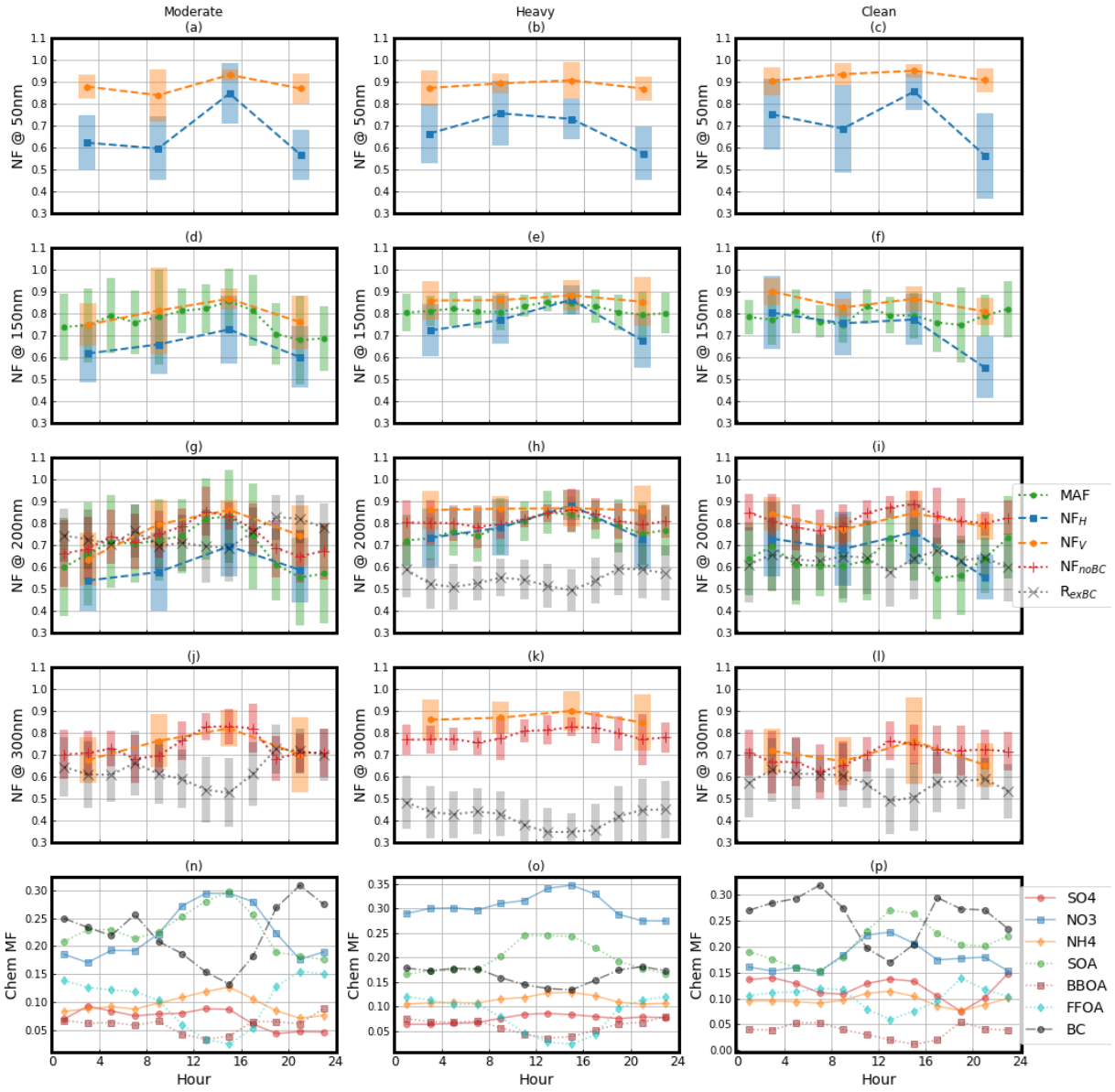

Figure 4. (a-l) Diurnal variations of aerosol mixing state parameters (identified by color and marker) at different particle sizes (50, 150, 200 and 300 nm) during the three periods. The shaded areas indicate the standard deviations. **MAF** (Maximum Activation Fraction): An asymptote of the measured SPAR curve at large particle. **NF_H**: Number Fraction of Hydrophilic aerosol whose hygroscopicity parameter is higher than ~0.07. **NF_V**: Number Fraction of Volatile aerosol whose Shrink Factor at 200 °C is lower than 0.85. **NF_{noBC}**: Number Fraction of BC-free particles. **R_{exBC}**: Number fraction of externally BC particles in total BC-containing particles. **(m-o)** Diurnal variations of mass fractions of aerosol chemical compositions including secondary organic aerosols (SOA), biomass burning organic aerosol (BBOA), fossil fuel organic aerosols (FFOA), and inorganic ions including sulfate (SO4), nitrate (NO3) and ammonium (NH4) (identified by color and marker) during the three periods.

The diurnal variations of MAF, NF_H, NF_V and NF_{noBC} along with the mass fractions of aerosol chemical components during the three periods, are shown in Fig.4. With the exception of particle size 50 nm, the diurnal variations of these four mixing state parameters were generally similar for all measured sizes. The different diurnal variations at particle size 50 nm may be due to the different effects of emissions and aging processes on different aerosol modes, as particles smaller than 100nm were mainly in a different aerosol mode (Aitken mode) to particles larger than 100nm (Wang et al., 2022). For particle sizes larger than 100 nm (shown in both Fig. 4 and Fig. S5), there were maxima in the afternoon for MAF, NF_H, NF_V and NF_{noBC}, indicative of a peak during this time due to the increase in secondary aerosol compositions like nitrate and SOA, and the decrease of POA and BC. The diurnal variations of aerosol mixing state parameters and aerosol chemical compositions were more pronounced in the moderately polluted period. During the heavily polluted period, the diurnal variation was least pronounced for NF_V and most pronounced for NF_H. In the clean period, there was another maxima at midnight for MAF and NF_{noBC}, which may be attributed to the diurnal variations of secondary aerosol compositions like sulfate and SOA, and the decrease of BC and FFOA. The average size-dependence of the aerosol mixing state parameters in different time ranges during the heavily polluted period is shown in Fig. S6. It can be seen that the differences among the four parameters were the least from 12:00 to 18:00, with the most SOA and the least POA. This is consistent with the results in Fig.3, where the difference between MAF and NF_H becomes smaller when POA fractions are the smallest. R_{exBC} tended to be lower during the daytime and its diurnal variation was more significant in larger particle sizes. In general, the diurnal variations for R_{exBC} are opposite to those of NF_{noBC} and agree better with those of the primary aerosol mass fractions. This is because BC particles originate from primary emissions and are mainly externally mixed. After experiencing aging process in the atmosphere, BC particles can be coated by secondary aerosol formed on, resulting in more coated BC particles and less externally mixed BC particles. As the secondary aerosol tends to form on larger particles, the diurnal variations of secondary aerosol formations may affect more significantly on those of mixing state of BC particles and thus RexBC in larger particle sizes.

The intercomparisons among MAF, NF_H, NF_V and NF_{noBC} were conducted based on their correlations at different particle sizes as summarized in Table. S1. Note that MAF at SSs of 0.08%, 0.14% and 0.22% was used for comparison at particle sizes of 200 nm, 150 nm and 100 nm. This is

because that the diameter range of rapid increases in SPAR curves are determined by aerosol hygroscopicity in this particle size range, and the midpoint of rapid increase diameter ranges of SPAR curves at SSs of 0.08%, 0.14% and 0.22% are approximately 180 nm, 120 nm and 90 nm (as shown in Fig. 2). In general, there were moderate correlations (r~0.5) among MAF, NF_H and NF_V, suggesting the dominance of CCN-active, hygroscopic and volatile aerosols are contributed by a similar particle group (Zhang et al., 2016). The agreement between MAF-NF_V was slightly higher than that of MAF-NF_H or NF_H-NF_V with similar correlation coefficients (~0.65) but smaller systematic differences (slope and intercept were much closer to 1 and 0, respectively), which is consistent with the previous finding that a substantial fraction of volatile but less hygroscopic aerosols is CCN-active. At smaller particle size, the correlation became weaker (r~0.4), while the degree of the reduction was the least for the correlation between MAF and NF_V.

3.3 Impacts of primary aerosol emissions on aerosol mixing states and parameter intercomparisons

In Fig. 5, the correlation between each aerosol mixing state parameter at 200 nm and the mass fraction of each primary organic aerosol composition during the three periods is presented. In general, these four mixing state parameters (MAF, NF_H, NF_V and NF_{noBC}) were negatively correlated with MF_{FFOA} and MF_{BBOA}. However, the correlation with MF_{FFOA} (-0.45~-0.74) was much weaker compared to MF_{BBOA} (-0.10~-0.45). Biomass burning emissions and fossil fuel emissions are two major sources of BC in the NCP (Yang et al., 2022), and NF_{noBC} was negatively correlated with MF_{FFOA} (r=-0.49) and weakly correlated (r=-0.18) with MF_{BBOA}, suggesting that fossil fuel emission were the more likely source of BC during this field campaign. The negative correlation between MAF and MF_{FFOA} was even weaker than that of NF_{noBC} with MF_{FFOA} (-0.62 vs. -0.49). Especially, at the same MF_{FFOA}, MAF was lower than NF_{noBC}, demonstrating that some BC-free particles were CCN-inactive, and likely mainly composed of organic aerosols from fossil fuel combustion emission. The negative correlation between NF_V and MF_{FFOA} was slightly weaker than that between NF_{noBC} and MF_{FFOA} (-0.56 vs -0.49). At the same MF_{FFOA}, NF_{noBC} was close to NF_V, and considering that BC-containing aerosols were dominated by thinly coated BC during most times (as shown in Fig.5), this demonstrates that the non-volatile population identified by the V-TDMA was mainly contributed by BC-containing

aerosols. NF_H had the lowest negative correlation with MF_{FFOA} (r=-0.74), demonstrating significant contributions from fossil fuel emissions to nearly hydrophobic aerosol populations. At the same MF_{FFOA}, the NF_H was obviously lower than NF_{noBC} (NF_H and NF_{noBC} are larger and smaller than 0.7 when MF_{FFOA} was larger than 0.1, respectively), demonstrating that a substantial portion of nearly

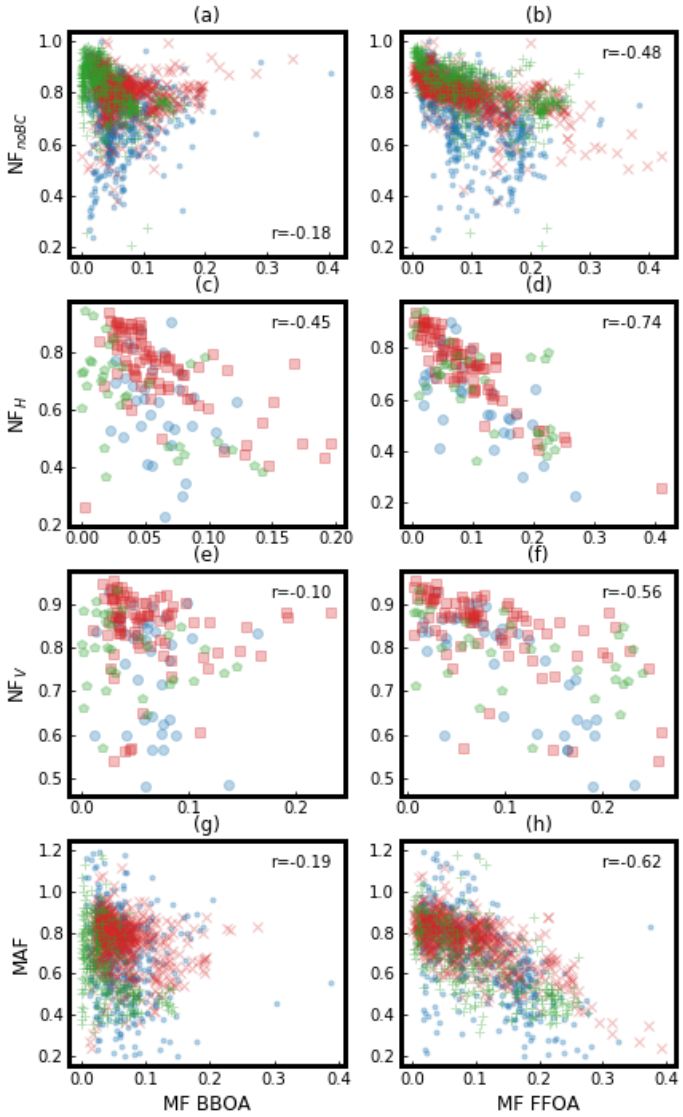

Figure 5. The correlations between aerosol mixing state parameters and mass fractions (MF) of BBOA (Biomass Burning Organic Aerosol) and FFOA (Fossil Fuel Organic Aerosol) during different periods (Moderately polluted period: Blue dot or circle; Heavily polluted period: Red x or square; Clean period: Green plus or pentagon.), with r representing correlation coefficient. **MAF** (Maximum Activation Fraction): An asymptote of the measured SPAR curve at large particle. **NF_H**: Number Fraction of Hydrophilic aerosol whose hygroscopicity parameter is higher than ~0.07. **NF_V**: Number Fraction of Volatile aerosol whose Shrink Factor at 200 °C is lower than 0.85. **NF_{noBC}**: Number Fraction of BC-free particles.

hydrophobic aerosols was not contributed by BC-containing aerosols, but likely by FFOA or BBOA

dominant aerosols (NF_H also had a negative correlation with MF_{BBOA}). However, the markedly different correlations between MAF with MF_{FFOA} (r=-0.62) and between MAF with MF_{BBOA} (r=-0.2) imply that those nearly hydrophobic but CCN-active aerosols were likely contributed by biomass burning emissions. The correlations between the ratio of thinly coated BC in total BC-containing particles (R_{exBC}) and the mass fractions of BBOA and FFOA are shown in Fig.6, and weak correlations ($r<0.3$) between R_{exBC} with MF_{BBOA} and MF_{FFOA} are observed. However, R_{exBC} tended to increase with MF_{FFOA}, suggesting that BC containing aerosols emitted from fossil fuel combustion tended to be more externally mixed with other aerosol components than those emitted from biomass burning activities. These results demonstrate remarkably different mixing states as well as physical and chemical properties of fossil fuel combustion aerosols and biomass burning aerosols.

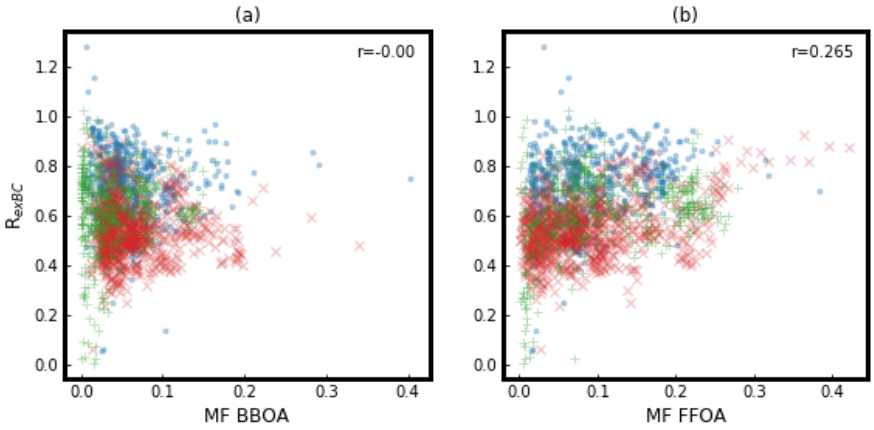

Figure. 6. The correlations between the ratio of external mixed BC in total BC particles (**R_{exBC}**) and mass fractions (MF) of **BBOA** (Biomass Burning Organic Aerosol) and **FFOA** (Fossil Fuel Organic Aerosol) during different periods (Moderately polluted period: Blue dot; Heavily polluted period: Red x; Clean period: Green plus), with r representing correlation coefficient.

The impact of primary emissions on the differences among the four aerosol mixing state parameters at particle size of 200 nm is analyzed and shown in Fig. 7. The difference between NF_{noBC} and NF_H (NF_{noBC}-NF_H) had significant positive correlations with MF_{FFOA} and MF_{BBOA} ($r>0.5$), suggesting that a substantial proportion of POA resided in BC-free aerosols and was volatile but contributed substantially to nearly hydrophobic aerosols. So did the difference between NF_V and NF_H (NF_V-NF_H). The mass fractions of BBOA and FFOA were poorly linked with the difference between MAF and NF_V (MAF-NF_V), or MAF and NF_{noBC} (MAF-NF_{noBC}), or NF_V and NF_{noBC} (NF_V-NF_{noBC}) (Fig. S7). The difference between MAF-NF_H had a positive correlation with MF_{BBOA}, further suggesting BBOA contributed to nearly hydrophobic aerosols under subsaturated conditions, however,

their hygroscopicity was enhanced and became CCN-active at supersaturated conditions. In addition, the correlation between mixing state parameters and primary aerosol composition during the campaign and different pollution periods were summarized in Fig. S7.

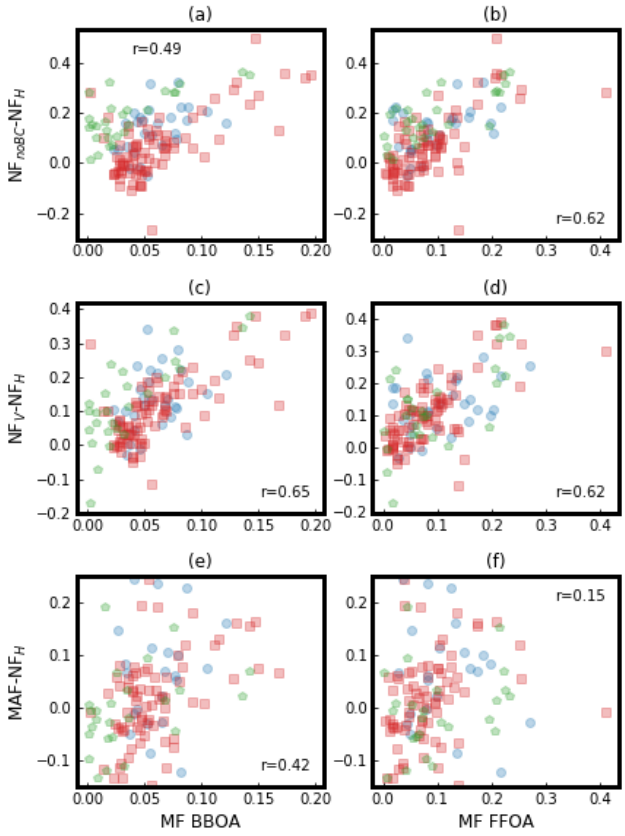

Figure 7. The correlations between the difference among the four aerosol mixing state parameters at particle size of 200 nm and mass fractions (MF) of **BBOA** (Biomass Burning Organic Aerosol) and **FFOA** (Fossil Fuel Organic Aerosol) during different periods (Moderately polluted period: Blue circle; Heavily polluted period: Red square; Clean period: Green pentagon), with r representing correlation coefficient. **NF_A-NF_B** (NF_{noBC}-NF_H, NF_V-NF_H, MAF -NF_H): The difference between the number fraction of A and B. **MAF** (Maximum Activation Fraction): An asymptote of the measured SPAR curve at large particle. **NF_H**: Number Fraction of Hydrophilic aerosol whose hygroscopicity parameter is higher than ~0.07. **NF_V**: Number Fraction of Volatile aerosol whose Shrink Factor at 200 °C is lower than 0.85. **NF_{noBC}**: Number Fraction of BC-free particles.

3.4 Impacts of secondary aerosol formations on aerosol mixing states and parameter intercomparisons

The correlations between each aerosol mixing state parameters at 200 nm and the mass fraction of each secondary aerosol (SA) component is presented in Fig. 8 for three periods and the entire

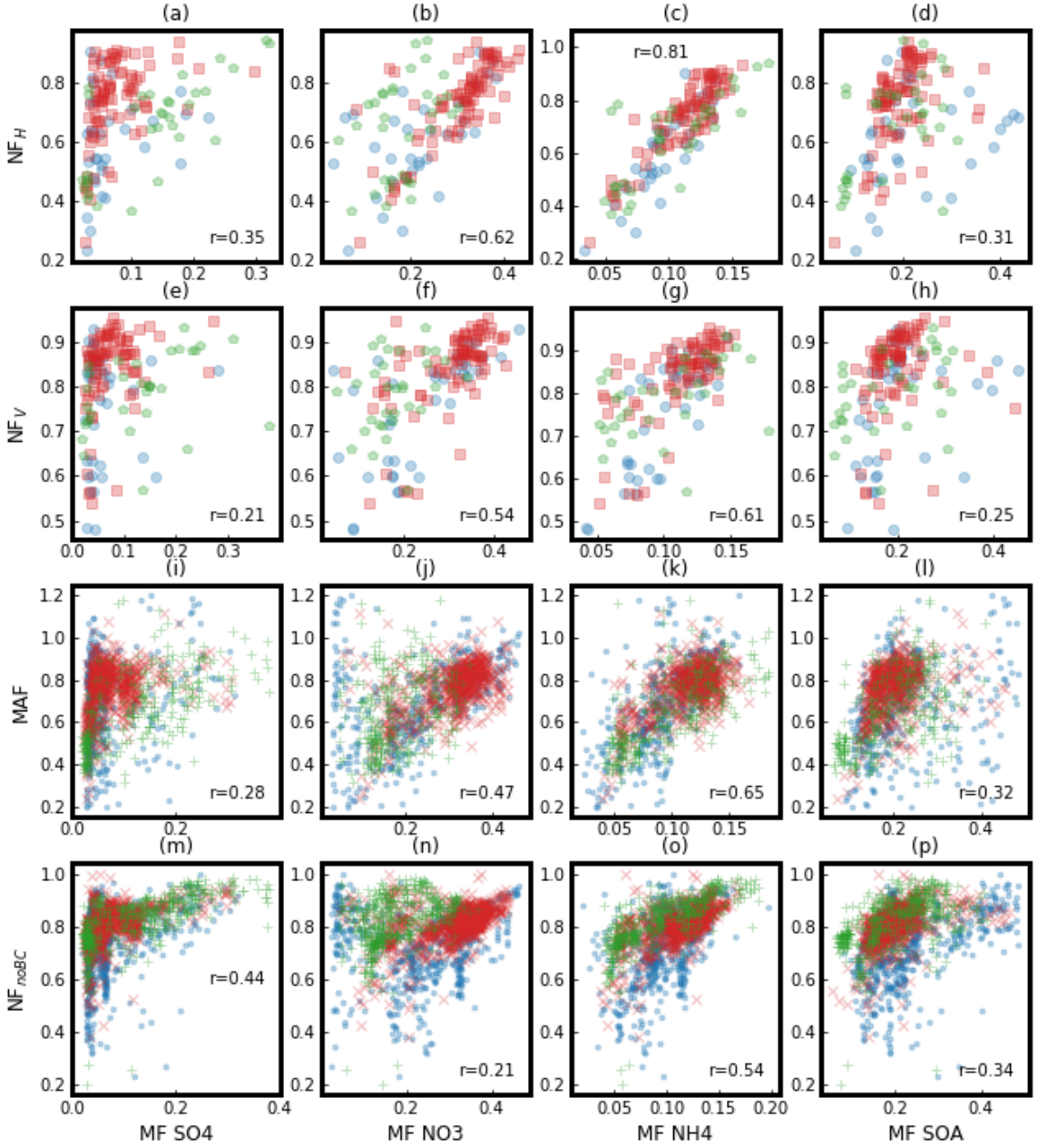

Figure 8. The correlation between the four aerosol mixing state parameters and mass fraction (MF) of secondary aerosol components during different periods (Moderately polluted period: Blue dot or circle; Heavily polluted period: Red x or square; Clean period: Green plus or pentagon.), with r representing correlation coefficient. **MAF** (Maximum Activation Fraction): An asymptote of the measured SPAR curve at large particle. $\mathbf{NF_H}$: Number Fraction of Hydrophilic aerosol whose hygroscopicity parameter is higher than ~0.07. $\mathbf{NF_V}$: Number Fraction of Volatile aerosol whose Shrink Factor at 200 °C is lower than 0.85. $\mathbf{NF_{noBC}}$: Number Fraction of BC-free particles. Secondary aerosol components including secondary organic aerosols (SOA), sulfate (SO4), nitrate (NO3) and ammonium (NH4).

campaign are presented. To be noted, in order to compare the four aerosol mixing state parameters as well as their relationships with aerosol chemical compositions at the same time, the analysis is

conducted at only 200 nm where all the four aerosol mixing state parameters were measured. Generally, MAF, NF_H, NF_V and NF_{noBC} had a strong positive correlation with MF_{NH4} (r>0.5). This is likely due to the fact that ammonium was mainly formed through the neutralization of sulfuric and nitric acid with ammonia, so variations in ammonium better represent overall secondary inorganic aerosol formation. As shown in Fig.3, the secondary inorganic aerosol components dominated over SA (about 50% vs about 70%), indicating that secondary aerosol formations were primarily composed of secondary inorganic aerosol formation, which explains the weaker correlations with SOA (r~0.3) seen in Fig. 8.

During the clean period when the mass fraction of SOA and sulfate were both above 15%, all four parameters had a strong positive correlation with MF_{SO4} and MF_{SOA} (r>0.5), suggesting that when clean background airmass with higher fractions of sulfate and SOA prevailed, local primary emissions that contributed substantially to BC-containing and less hygroscopic POA aerosols became less significant. The positive correlations between MAF and secondary aerosol components have been extensively discussed by Tao et al. (2021), who found that secondary aerosol formations enhance the hygroscopicity of nearly hydrophobic aerosols, thereby increasing CCN activity. This also explains the highest correlations of NF_H or MAF with ammonium formation. The strong positive correlations between NF_V and secondary aerosol formations (r~0.6) are consistent with the fact that nitrate dominates secondary aerosol formations during this campaign and nitrate is semi-volatile. For the first time, the strong positive correlations between NF_{noBC} and secondary aerosol formations were revealed (r~0.6). This is because NF_{noBC} primarily depends on the relative variations of BC-containing and BC-free aerosols. The increase in NF_{noBC} at 200 nm as a function of secondary aerosol mass fraction suggests that secondary aerosol formations migrated a higher fraction of BC-free aerosols smaller than 200 nm to 200 nm, highlighting that secondary aerosols tended to form more quickly on BC-free aerosols than on BC-containing aerosols.

The effects of secondary aerosol formation on the differences between the four aerosol mixing state parameters were studied and illustrated in Fig. 9. To be noted, two OOA factors (OOA1 and OOA2) resulted from different chemical processing are identified. Differences between NF_{noBC} and NF_H (NF_{noBC}-NF_H) showed a strong negative correlation with MF_{NH4} and MF_{NO3} (mainly -0.6). So did

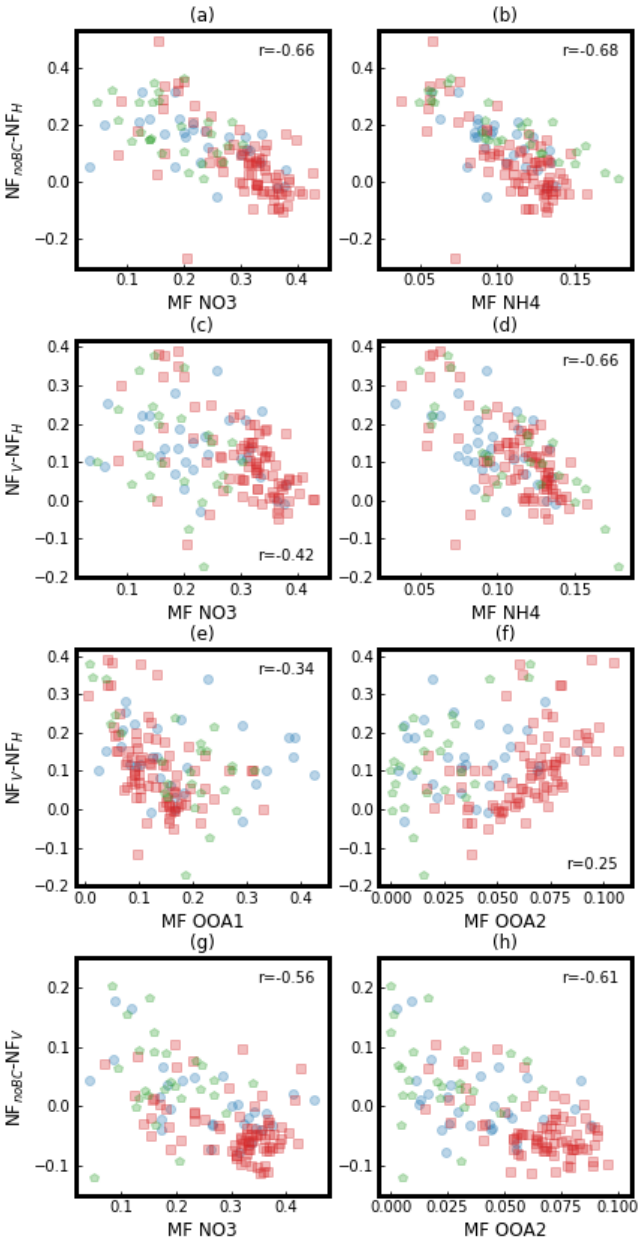

Figure 9. The correlation between the difference among the four aerosol mixing state parameters and mass fractions (MF) of secondary aerosol chemical components during different periods. OOA1 and OOA2 are two SOA factors resolved from AMS measurements using the PMF technique. Moderately polluted period: Blue circle; Heavily polluted period: Red square; Clean period: Green pentagon. **NF_A-NF_B** (NF_{noBC}-NF_H, NF_V-NF_H, NF_{noBC}-NF_V): The difference between the number fraction of A and B. **NF_H**: Number Fraction of Hydrophilic aerosol whose hygroscopicity parameter is higher than ~0.07. **NF_V**: Number Fraction of Volatile aerosol whose Shrink Factor at 200 °C is lower than 0.85. **NF_{noBC}**: Number Fraction of BC-free particles.

the difference between NF_V and NF_H (NF_V-NF_H). As previously noted , NF_H typically had smaller values than NF_V and NF_{noBC}. Thus, a negative correlation with the mass fraction of ammonium and nitrate indicates that the formation of secondary nitrate results in a smaller difference between these mixing state parameters. The increase in the fraction of ammonium nitrate, a pure scattering semi-

volatile compound with strong hygroscopicity, can render the aerosol population more dominated by particles with strong volatility and hygroscopicity. This can result in a smaller difference between NF_{noBC}, $NF_{H,}$ and NF_V as the secondary inorganic aerosol components increases. Furthermore, the difference between NF_V-NF_H showed a positive correlation with MF_{OOA2} and a negative correlation with MF_{OOA1}, indicating different volatility and hygroscopicity of the two SOA factors. The variations in the difference between NF_V and NF_H with the mass fraction of OOA1 and OOA2 are shown in Fig. 9(e) and (f). As previously noted, NF_V was generally higher than NF_H, and the difference between the two decreases with an increase in $MF_{OOA1,}$ which were generally smaller than 0.3. This suggests that the formation of OOA1 enhances the hygroscopicity of volatile particles, which aligns with the highest oxidation state of OOA1 (higher O/C but lower H/C compared to OOA2), which had significant and overall positive impact on aerosol hygroscopicity (Cerully et al., 2015; Thalman et al., 2017; Zhang et al., 2023). A positive correlation is seen between NF_V and MF_{OOA2} (r=~0.25), whereas the correlation between NF_H and MF_{OOA2} is weak (R is close to 0), implying that OOA2 might be semi-volatile but only weakly hygroscopic, which could contribute to NF_V being higher than NF_H as OOA1 increases. The difference between NF_{noBC} and NF_V (NF_{noBC}-NF_V) is negatively correlated with MF_{NO3}, which is consistent with the semi-volatile nature of nitrate. The negative correlation between NF_{noBC}-NF_V and MF_{OOA2} indicates that the difference is smaller when there is more OOA2, implying that OOA2 are also semi-volatile compounds and were likely formed mainly on BC-free particles. The correlations between the difference between NF_V-MAF and NF_{noBC}-MAF and the mass fraction of each secondary aerosol composition are much weak. The impacts of secondary aerosol formation on BC mixing states are depicted in Fig. S8. In general, the number fraction of thinly coated BC has a negative correlation with SIA and a weak association with SOA, suggesting that SIA formation mainly enhances the thickness of BC coating. Besides, the correlation between mixing state parameters and secondary aerosol composition during the campaign and different pollution periods were summarized in Fig. S9.

In addition to the changes in the mass fractions of secondary aerosol compositions, the accumulation of pollution due to secondary aerosols may also provide insight into the impact of secondary aerosol formations on aerosol mixing states. As shown in Fig. 10 (a), during the heavily polluted periods, there were two distinct pollution accumulation processes from Oct 23rd to Oct 27th

585 and from Oct 28rd to Oct 31st, respectively. During the pollution accumulation process, the mass
586 concentration of secondary aerosols increased by approximately three times, indicating rapid
587 formation of secondary compositions and causing a significant rise in non-refractory PM_1 (NR-PM_1)

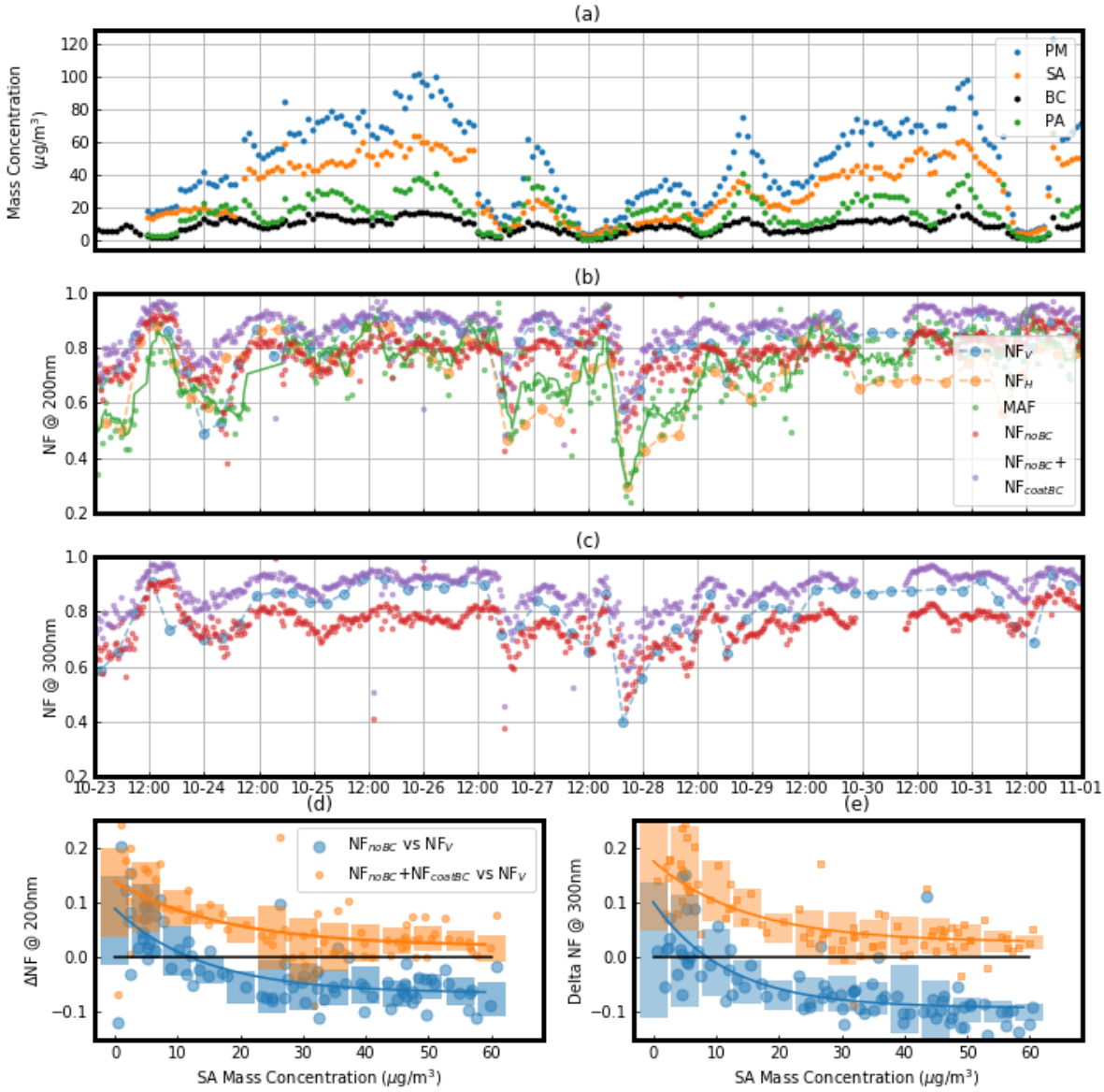

Figure 10. The variations of different aerosol mixing state parameters during the pollution accumulation process. **(a)** The time series of mass concentrations of non-refractory PM_1 (NR-PM_1), secondary aerosols (SA, including inorganic ions and SOA), primary organic aerosols (POA) and BC (identified by colors and markers). **(b and c)** The variations of different aerosol mixing state parameters (identified by colors and markers) at particle size of 200nm **(b)** and 300nm **(c)**; **(d and e)** The variations of the difference between NF_V and NF_{noBC} (NF_V-NF_{noBC}, blue large circle) and the difference between NF_V and NF_{noBC}+NF_{CBC} (NF_V-(NF_{noBC}+NF_{CBC}), yellow small circle) with the mass concentration of SA at particle size of 200nm **(d)** and 300nm **(e)**. **MAF** (Maximum Activation Fraction): An asymptote of the measured SPAR curve at large particle. **NF_H**: Number Fraction of Hydrophilic aerosol whose hygroscopicity parameter is higher than ~0.07. **NF_V**: Number Fraction of Volatile aerosol whose Shrink Factor at 200 °C is lower than 0.85. **NF_{CBC}:** Number Fraction of thickly coated BC particles.

mass concentration. Fig. 10 (b and c) illustrates that this increase in secondary aerosols led to a significant enhancement of aerosol mixing state parameters, including MAF, NF_V, NF_H and NF_{noBC}, which rose from about 0.5 to about 0.8 with evident diurnal variations. This highlights the impact of secondary aerosol formations on aerosol mixing states and the importance of studying the pollution accumulation processes of secondary aerosols. The enhancements of different aerosol mixing state parameters during the pollution accumulation process were not uniform. MAF and NF_H initially showed lower values compared to NF_V and NF_{noBC}, but their later enhancement was stronger than that of NF_{noBC}. Fig. 10 (d) and (e) show the difference between NF_{noBC} and NF_V at 200 nm and 300 nm as a function of secondary aerosol mass concentrations during these two pollution periods, which clearly displays how during secondary aerosol formations NF_V became higher than NF_{noBC} while NF_V kept close to the number fraction of thickly coated BC containing aerosols (NF_{CBC}) plus NF_{noBC} (NF_{CBC}+NF_{CBC}). The results suggest that secondary aerosol formation increases the volatility of BC-free and BC-containing aerosols, leading increased NF_V compared to NF_{noBC}. And almost all BC-free particles and some BC-containing aerosols became volatile during the pollution accumulation process.

4. Conclusions

The aerosol mixing state is one of the most important physicochemical properties of aerosol particles, which has significant impacts on the optical properties and CCN activity of aerosol particles. Aerosol mixing states vary largely under complex aerosol emissions and atmospheric transformations. In this study, aerosol mixing states derived from CCN activity, hygroscopicity, volatility and BC particles observations, along with their relationship to primary aerosols emissions and secondary aerosol formations, were systematically analyzed based on simultaneous measurements of a CCNC, a H/VTDMA and a SP2. Statistical analysis demonstrated that the number fraction of CCN-active, hygroscopic and volatile particles was generally positively correlated to one another and were contributed mainly by BC-free aerosols. Therefore, the four mixing state parameters (**NF_{noBC}**: Number Fraction of BC-free particles, **MAF**: Maximum Activation Fraction. **NF_H**: Number Fraction of Hydrophilic aerosol whose hygroscopicity parameter is higher than ~0.07. **NF_V**: Number Fraction of Volatile aerosol whose Shrink Factor at 200 °C is lower than 0.85.) were all negatively correlated to either mass fractions of BBOA (Biomass Burning Organic Aerosols) or FFOA (Fossil Fuel Organic

Aerosols), because fossil fuel combustion and biomass burning were two major sources of BC-containing aerosols during this field campaign. However, differences among these mixing state parameters varied much under different conditions.

The intercomparison results highlight the differences in aerosol mixing states and physiochemical properties caused by fossil fuel combustion and biomass burning emissions. CCN and SP2 measurements showed that CCN-inactive, BC-free particles were mainly produced by fossil fuel combustion. On the other hand, the comparison between VTDMA and SP2 measurements indicated that non-volatile aerosols were mostly composed of BC-containing particles. The comparison between HTDMA and SP2 measurements revealed that a significant proportion of nearly hydrophobic aerosols was not from BC-containing particles, but from fossil fuel combustion or biomass burning dominated organic aerosols. The correlation between CCNC and HTDMA measurements also showed that nearly hydrophobic, BC-free aerosols can become CCN-active under supersaturated conditions and were tightly linked to biomass burning emissions. This suggests that biomass burning aerosols might exhibit different hygroscopicity under sub- and super- saturated conditions (Bougiatioti et al., 2016). Furthermore, the correlation analysis between SP2 measurements and mass fractions of BBOA and FFOA indicated that BC-containing aerosols from fossil fuel combustion tend to be more externally mixed with other aerosol compositions compared to those from biomass burning activities.

Other than primary aerosol emissions, secondary aerosol formations also exerted significant impacts on variations of aerosol mixing states. During this campaign, the secondary aerosol formation was dominated by nitrate and SOA production, which have markedly different impacts on aerosol mixing states due to their different physical properties and formation pathways. NF_{noBC}, MAF, $NF_{H,}$ and NF_{V} were all positively correlated with nitrate and SOA mass fractions, revealing much stronger correlations to SOA than with nitrate. This is consistent with the semi-volatile but highly hygroscopic properties of nitrate. The high correlation coefficient between NF_{noBC} and the mass fractions of secondary aerosols at 200 nm and 300 nm suggests that secondary aerosol formation led to the migration of BC-free aerosols towards larger diameters more quickly than BC-containing aerosols. This outcome reveals that secondary aerosols formed more rapidly on BC-free aerosols than on BC-containing aerosols, which is in line with the BC-containing aerosols' hydrophobic nature that does not favor aqueous secondary aerosol formation. Moreover, as the mass fractions of nitrate or

ammonium increased, the differences among mixing state parameters (NF_{noBC}, MAF, NF_H and NF_V) mostly decreased due to the hygroscopic and semi-volatile nature of ammonium nitrate. However, the two resolved SOA factors exhibited different impacts on the difference between NF_V and NF_H (NF_V-NF_H), and their correlations with NF_V and NF_H revealed that OOA1 was more hygroscopic but less volatile, suggesting distinct formation mechanisms for the two OOA factors during the field campaign.

The findings of this study highlight markedly different effects of primary emissions and secondary aerosol formations on aerosol mixing states and suggest that comparisons of aerosol mixing states obtained using various techniques are useful for gaining insights into the hygroscopicity, volatility, and CCN activity of different aerosols. These comparisons can also indicate the impacts of secondary aerosol formations on aerosol physical properties, which can help to understand the pathways of secondary aerosol formation. However, it is important to be cautious in the application of aerosol mixing state parameters, as the suitability of VTDMA-derived mixing state parameters in representing BC mixing states is largely dependent on the composition and mass of secondary aerosols.

Data availability. The data used in this study are available from the corresponding author upon request Ye Kuang (kuangye@jnu.edu.cn) and Li Liu (liul@gd121.cn)

Competing interests. The authors declare that they have no conflict of interest.

Author Contributions.

YK and WY planned this campaign and YK designed the aerosol experiments and conceived this research together with JC, and JC wrote the manuscript. JC performed measurements of CCNC, BL performed measurements of SP2 and analyzed SP2 datasets with the help of GZ, WQ and YL performed AMS measurements, LL performed HV-TDMA measurements and conducted post-data processing as well as some of data analysis. BX, HX, MMZ, HZ and SR participated this campaign and helped instruments maintenance. GZ provided full support for the campaign. All authors contributed to discussions and revisions of this paper.

Financial supports. This work is supported by National Natural Science Foundation of China (42175083, 42175127, 42275066). The Guangdong Provincial Key Research and Development Program (grant no. 2020B1111360003), the Science and Technology Innovation Team Plan of Guangdong Meteorological Bureau (grant no. GRMCTD202003).

References

Adachi, K., Sedlacek, A. J., Kleinman, L., Chand, D., Hubbe, J. M., and Buseck, P. R.: Volume changes upon heating of aerosol particles from biomass burning using transmission electron microscopy, Aerosol Science and Technology, 52, 46–56, https://doi.org/10.1080/02786826.2017.1373181, 2018.

Adachi, K., Sedlacek, A. J., Kleinman, L., Springston, S. R., Wang, J., Chand, D., Hubbe, J. M., Shilling, J. E., Onasch, T. B., Kinase, T., Sakata, K., Takahashi, Y., and Buseck, P. R.: Spherical tarball particles form through rapid chemical and physical changes of organic matter in biomass-burning smoke, Proceedings of the National Academy of Sciences, 116, 19336–19341, https://doi.org/10.1073/pnas.1900129116, 2019.

Bond, T. C., Doherty, S. J., Fahey, D. W., Forster, P. M., Berntsen, T., DeAngelo, B. J., Flanner, M. G., Ghan, S., Kaercher, B., Koch, D., Kinne, S., Kondo, Y., Quinn, P. K., Sarofim, M. C., Schultz, M. G., Schulz, M., Venkataraman, C., Zhang, H., Zhang, S., Bellouin, N., Guttikunda, S. K., Hopke, P. K., Jacobson, M. Z., Kaiser, J. W., Klimont, Z., Lohmann, U., Schwarz, J. P., Shindell, D., Storelvmo, T., Warren, S. G., and Zender, C. S.: Bounding the role of black carbon in the climate system: A scientific assessment, Journal of Geophysical Research-Atmospheres, 118, 5380–5552, https://doi.org/10.1002/jgrd.50171, 2013.

Bougiatioti, A., Bezantakos, S., Stavroulas, I., Kalivitis, N., Kokkalis, P., Biskos, G., Mihalopoulos, N., Papayannis, A., and Nenes, A.: Biomass-burning impact on CCN number, hygroscopicity and cloud formation during summertime in the eastern Mediterranean, Atmos. Chem. Phys., 16, 7389–7409, https://doi.org/10.5194/acp-16-7389-2016, 2016.

Cai, M., Tan, H., Chan, C. K., Mochida, M., Hatakeyama, S., Kondo, Y., Schurman, M. I., Xu, H., Li, F., Shimada, K., Li, L., Deng, Y., Yai, H., Matsuki, A., Qin, Y., and Zhao, J.: Comparison of Aerosol Hygroscopcity, Volatility, and Chemical Composition between a Suburban Site in the Pearl River Delta Region and a Marine Site in Okinawa, Aerosol and Air Quality Research, 17, 3194–3208, https://doi.org/10.4209/aaqr.2017.01.0020, 2017.

Canagaratna, M. R., Jimenez, J. L., Kroll, J. H., Chen, Q., Kessler, S. H., Massoli, P., Hildebrandt Ruiz, L., Fortner, E., Williams, L. R., Wilson, K. R., Surratt, J. D., Donahue, N. M., Jayne, J. T., and Worsnop, D. R.: Elemental ratio measurements of organic compounds using aerosol mass spectrometry: characterization, improved calibration, and implications, Atmos. Chem. Phys., 15, 253–272, https://doi.org/10.5194/acp-15-253-2015, 2015.

Cerully, K. M., Bougiatioti, A., Hite Jr., J. R., Guo, H., Xu, L., Ng, N. L., Weber, R., and Nenes, A.: On the link between hygroscopicity, volatility, and oxidation state of ambient and water-soluble aerosols in the southeastern United States, Atmos. Chem. Phys., 15, 8679–8694, https://doi.org/10.5194/acp-15-8679-2015, 2015.

Chen, C., Qiu, Y., Xu, W., He, Y., Li, Z., Sun, J., Ma, N., Xu, W., Pan, X., Fu, P., Wang, Z., and Sun, Y.: Primary Emissions and Secondary Aerosol Processing During Wintertime in Rural Area of North China Plain, Journal of Geophysical Research: Atmospheres, 127, e2021JD035430, https://doi.org/10.1029/2021JD035430, 2022.

Chen, J., Budisulistiorini, S. H., Miyakawa, T., Komazaki, Y., and Kuwata, M.: Secondary aerosol formation promotes water uptake by organic-rich wildfire haze particles in equatorial Asia, Atmos. Chem. Phys., 18, 7781–7798, https://doi.org/10.5194/acp-18-7781-2018, 2018.

Cheng, Y. F., Su, H., Rose, D., Gunthe, S. S., Berghof, M., Wehner, B., Achtert, P., Nowak, A., Takegawa, N., Kondo, Y., Shiraiwa, M., Gong, Y. G., Shao, M., Hu, M., Zhu, T., Zhang, Y. H., Carmichael, G. R., Wiedensohler, A., Andreae, M. O., and Pöschl, U.: Size-resolved measurement of the mixing state of soot in the megacity Beijing, China: diurnal cycle, aging and parameterization, Atmos. Chem. Phys., 12, 4477–4491, https://doi.org/10.5194/acp-12-4477-2012, 2012.

Ching, J., Fast, J., West, M., and Riemer, N.: Metrics to quantify the importance of mixing state for CCN activity, Atmos. Chem. Phys., 17, 7445–7458, https://doi.org/10.5194/acp-17-7445-2017, 2017.

Ching, J., Adachi, K., Zaizen, Y., Igarashi, Y., and Kajino, M.: Aerosol mixing state revealed by transmission electron microscopy pertaining to cloud formation and human airway deposition, npj Climate and Atmospheric Science, 2, 22, https://doi.org/10.1038/s41612-019-0081-9, 2019.

Deng, Z. Z., Zhao, C. S., Ma, N., Liu, P. F., Ran, L., Xu, W. Y., Chen, J., Liang, Z., Liang, S., Huang, M. Y., Ma, X. C., Zhang, Q., Quan, J. N., Yan, P., Henning, S., Mildenberger, K., Sommerhage, E., Schäfer, M., Stratmann, F., and Wiedensohler, A.: Size-resolved and bulk activation properties of aerosols in the North China Plain, Atmos. Chem. Phys., 11, 3835–3846, https://doi.org/10.5194/acp-11-3835-2011, 2011.

Deng, Z. Z., Zhao, C. S., Ma, N., Ran, L., Zhou, G. Q., Lu, D. R., and Zhou, X. J.: An examination of parameterizations for the CCN number concentration based on in situ measurements of aerosol activation properties in the North China Plain, Atmos. Chem. Phys., 13, 6227–6237, https://doi.org/10.5194/acp-13-6227-2013, 2013.

Drinovec, L., Močnik, G., Zotter, P., Prévôt, A. S. H., Ruckstuhl, C., Coz, E., Rupakheti, M., Sciare, J., Müller, T., Wiedensohler, A., and Hansen, A. D. A.: The "dual-spot" Aethalometer: an improved measurement of aerosol black carbon with real-time loading compensation, Atmos. Meas. Tech., 8, 1965–1979, https://doi.org/10.5194/amt-8-1965-2015, 2015.

Ervens, B.: Modeling the Processing of Aerosol and Trace Gases in Clouds and Fogs, Chemical Reviews, 115, 4157–4198, https://doi.org/10.1021/cr5005887, 2015.

Farmer, D. K., Cappa, C. D., and Kreidenweis, S. M.: Atmospheric Processes and Their Controlling Influence on Cloud Condensation Nuclei Activity, Chemical Reviews, 115, 4199–4217, https://doi.org/10.1021/cr5006292, 2015.

Fierce, L., Riemer, N., and Bond, T. C.: Toward Reduced Representation of Mixing State for Simulating Aerosol Effects on Climate, Bulletin of the American Meteorological Society, 98, 971–980, https://doi.org/10.1175/BAMS-D-16-0028.1, 2017.

Fu, Y., Peng, X., Sun, W., Hu, X., Wang, D., Yang, Y., Guo, Z., Wang, Y., Zhang, G., Zhu, J., Ou, J., Shi, Z., Wang, X., and Bi, X.: Impact of Cloud Process in the Mixing State and Microphysical Properties of Soot Particles: Implications in Light Absorption Enhancement, Journal of Geophysical Research: Atmospheres, n/a, e2022JD037169, https://doi.org/10.1029/2022JD037169, 2022.

Gysel, M., Laborde, M., Olfert, J. S., Subramanian, R., and Gröhn, A. J.: Effective density of Aquadag and fullerene soot black carbon reference materials used for SP2 calibration, Atmos. Meas. Tech., 4, 2851–2858, https://doi.org/10.5194/amt-4-2851-2011, 2011.

Herich, H., Kammermann, L., Gysel, M., Weingartner, E., Baltensperger, U., Lohmann, U., and Cziczo, D. J.: In situ determination of atmospheric aerosol composition as a function of hygroscopic growth, Journal of Geophysical Research: Atmospheres, 113, https://doi.org/10.1029/2008JD009954, 2008.

Herich, H., Kammermann, L., Friedman, B., Gross, D. S., Weingartner, E., Lohmann, U., Spichtinger, P., Gysel, M., Baltensperger, U., and Cziczo, D. J.: Subarctic atmospheric aerosol composition: 2. Hygroscopic growth properties, Journal of Geophysical Research: Atmospheres, 114, https://doi.org/10.1029/2008JD011574, 2009.

Hong, J., Äijälä, M., Häme, S. A. K., Hao, L., Duplissy, J., Heikkinen, L. M., Nie, W., Mikkilä, J., Kulmala, M., Prisle, N. L., Virtanen, A., Ehn, M., Paasonen, P., Worsnop, D. R., Riipinen, I., Petäjä, T., and Kerminen, V.-M.: Estimates of the organic aerosol volatility in a boreal forest using two independent methods, Atmos. Chem. Phys., 17, 4387–4399, https://doi.org/10.5194/acp-17-4387-2017, 2017.

Jayne, J. T., Leard, D. C., Zhang, X., Davidovits, P., Smith, K. A., Kolb, C. E., and Worsnop, D. R.: Development of an Aerosol Mass Spectrometer for Size and Composition Analysis of Submicron Particles, Aerosol Science and Technology, 33, 49–70, https://doi.org/10.1080/027868200410840, 2000.

Jiang, X., Tao, J., Kuang, Y., Hong, J., and Ma, N.: Mathematical derivation and physical interpretation of particle size-resolved activation ratio based on particle hygroscopicity distribution: Application on global characterization of CCN activity, Atmospheric Environment, 246, 118137, https://doi.org/10.1016/j.atmosenv.2020.118137, 2021.

Jurányi, Z., Tritscher, T., Gysel, M., Laborde, M., Gomes, L., Roberts, G., Baltensperger, U., and Weingartner, E.: Hygroscopic mixing state of urban aerosol derived from size-resolved cloud condensation nuclei measurements during the MEGAPOLI campaign in Paris, Atmos. Chem. Phys., 13, 6431–6446, https://doi.org/10.5194/acp-13-6431-2013, 2013.

Kawana, K., Nakayama, T., and Mochida, M.: Hygroscopicity and CCN activity of atmospheric aerosol particles and their relation to organics: Characteristics of urban aerosols in Nagoya, Japan, Journal of Geophysical Research: Atmospheres, 121, 4100–4121, https://doi.org/10.1002/2015jd023213, 2016.

Kim, N., Yum, S. S., Park, M., Park, J. S., Shin, H. J., and Ahn, J. Y.: Hygroscopicity of urban aerosols and its link to size-resolved chemical composition during spring and summer in Seoul, Korea, Atmos. Chem. Phys., 20, 11245–11262, https://doi.org/10.5194/acp-20-11245-2020, 2020.

Kuang, Y., Zhao, C. S., Tao, J. C., and Ma, N.: Diurnal variations of aerosol optical properties in the North China Plain and their influences on the estimates of direct aerosol radiative effect, Atmos. Chem. Phys., 15, 5761–5772, https://doi.org/10.5194/acp-15-5761-2015, 2015.

Kuang, Y., He, Y., Xu, W., Yuan, B., Zhang, G., Ma, Z., Wu, C., Wang, C., Wang, S., Zhang, S., Tao, J., Ma, N., Su, H., Cheng, Y., Shao, M., and Sun, Y.: Photochemical Aqueous-Phase Reactions

Induce Rapid Daytime Formation of Oxygenated Organic Aerosol on the North China Plain, Environmental Science & Technology, 54, 3849–3860, https://doi.org/10.1021/acs.est.9b06836, 2020.

Kuang, Y., Huang, S., Xue, B., Luo, B., Song, Q., Chen, W., Hu, W., Li, W., Zhao, P., Cai, M., Peng, Y., Qi, J., Li, T., Wang, S., Chen, D., Yue, D., Yuan, B., and Shao, M.: Contrasting effects of secondary organic aerosol formations on organic aerosol hygroscopicity, Atmos. Chem. Phys., 21, 10375–10391, https://doi.org/10.5194/acp-21-10375-2021, 2021.

Kuwata, M. and Kondo, Y.: Dependence of size-resolved CCN spectra on the mixing state of nonvolatile cores observed in Tokyo, Journal of Geophysical Research: Atmospheres, 113, https://doi.org/10.1029/2007JD009761, 2008.

Kuwata, M., Kondo, Y., Mochida, M., Takegawa, N., and Kawamura, K.: Dependence of CCN activity of less volatile particles on the amount of coating observed in Tokyo, Journal of Geophysical Research: Atmospheres, 112, https://doi.org/10.1029/2006JD007758, 2007.

Lack, D. A., Langridge, J. M., Bahreini, R., Cappa, C. D., Middlebrook, A. M., and Schwarz, J. P.: Brown carbon and internal mixing in biomass burning particles, Proceedings of the National Academy of Sciences, 109, 14802–14807, https://doi.org/10.1073/pnas.1206575109, 2012.

Lance, S., Nenes, A., Medina, J., and Smith, J. N.: Mapping the operation of the DMT continuous flow CCN counter, Aerosol science and technology, 40, 242–254, 2006.

Lance, S., Raatikainen, T., Onasch, T. B., Worsnop, D. R., Yu, X. Y., Alexander, M. L., Stolzenburg, M. R., McMurry, P. H., Smith, J. N., and Nenes, A.: Aerosol mixing state, hygroscopic growth and cloud activation efficiency during MIRAGE 2006, Atmos. Chem. Phys., 13, 5049–5062, https://doi.org/10.5194/acp-13-5049-2013, 2013.

Lata, N. N., Zhang, B., Schum, S., Mazzoleni, L., Brimberry, R., Marcus, M. A., Cantrell, W. H., Fialho, P., Mazzoleni, C., and China, S.: Aerosol Composition, Mixing State, and Phase State of Free Tropospheric Particles and Their Role in Ice Cloud Formation, ACS Earth Space Chem., 5, 3499–3510, https://doi.org/10.1021/acsearthspacechem.1c00315, 2021.

Lee, A. K. Y., Rivellini, L.-H., Chen, C.-L., Liu, J., Price, D. J., Betha, R., Russell, L. M., Zhang, X., and Cappa, C. D.: Influences of Primary Emission and Secondary Coating Formation on the Particle Diversity and Mixing State of Black Carbon Particles, Environ. Sci. Technol., 53, 9429–9438, https://doi.org/10.1021/acs.est.9b03064, 2019.

Li, G., Su, H., Ma, N., Tao, J., Kuang, Y., Wang, Q., Hong, J., Zhang, Y., Kuhn, U., and Zhang, S.: Multiphase chemistry experiment in Fogs and Aerosols in the North China Plain (McFAN): integrated analysis and intensive winter campaign 2018, Faraday Discussions, 2021.

Liu, D., Joshi, R., Wang, J., Yu, C., Allan, J. D., Coe, H., Flynn, M. J., Xie, C., Lee, J., Squires, F., Kotthaus, S., Grimmond, S., Ge, X., Sun, Y., and Fu, P.: Contrasting physical properties of black carbon in urban Beijing between winter and summer, Atmos. Chem. Phys., 19, 6749–6769, https://doi.org/10.5194/acp-19-6749-2019, 2019.

Liu, D., Li, S., Hu, D., Kong, S., Cheng, Y., Wu, Y., Ding, S., Hu, K., Zheng, S., Yan, Q., Zheng, H., Zhao, D., Tian, P., Ye, J., Huang, M., and Ding, D.: Evolution of Aerosol Optical Properties from Wood Smoke in Real Atmosphere Influenced by Burning Phase and Solar Radiation, Environ. Sci. Technol., 55, 5677–5688, https://doi.org/10.1021/acs.est.0c07569, 2021.

Liu, K., Zhang, C., Cheng, Y., Liu, C., Zhang, H., Zhang, G., Sun, X., and Mu, Y.: Serious BTEX pollution in rural area of the North China Plain during winter season, Journal of Environmental Sciences, 30, 186–190, https://doi.org/10.1016/j.jes.2014.05.056, 2015.

Liu, P. F., Zhao, C. S., Göbel, T., Hallbauer, E., Nowak, A., Ran, L., Xu, W. Y., Deng, Z. Z., Ma, N., and Mildenberger, K.: Hygroscopic properties of aerosol particles at high relative humidity and their diurnal variations in the North China Plain, Atmos. Chem. Phys, 11, 3479–3494, 2011.

Luo, B., Kuang, Y., Huang, S., Song, Q., Hu, W., Li, W., Peng, Y., Chen, D., Yue, D., Yuan, B., and Shao, M.: Parameterizations of size distribution and refractive index of biomass burning organic aerosol with black carbon content, Atmos. Chem. Phys., 22, 12401–12415, https://doi.org/10.5194/acp-22-12401-2022, 2022.

Ma, N., Zhao, C. S., Müller, T., Cheng, Y. F., Liu, P. F., Deng, Z. Z., Xu, W. Y., Ran, L., Nekat, B., van Pinxteren, D., Gnauk, T., Müller, K., Herrmann, H., Yan, P., Zhou, X. J., and Wiedensohler, A.: A new method to determine the mixing state of light absorbing carbonaceous using the measured aerosol optical properties and number size distributions, Atmos. Chem. Phys., 12, 2381–2397, https://doi.org/10.5194/acp-12-2381-2012, 2012.

Ma, N., Zhao, C., Tao, J., Wu, Z., Kecorius, S., Wang, Z., Größ, J., Liu, H., Bian, Y., Kuang, Y., Teich, M., Spindler, G., Müller, K., van Pinxteren, D., Herrmann, H., Hu, M., and Wiedensohler, A.: Variation of CCN activity during new particle formation events in the North China Plain, Atmos. Chem. Phys., 16, 8593–8607, https://doi.org/10.5194/acp-16-8593-2016, 2016.

Matsui, H., Hamilton, D. S., and Mahowald, N. M.: Black carbon radiative effects highly sensitive to emitted particle size when resolving mixing-state diversity, Nature Communications, 9, 3446, https://doi.org/10.1038/s41467-018-05635-1, 2018.

Mei, F., Hayes, P. L., Ortega, A., Taylor, J. W., Allan, J. D., Gilman, J., Kuster, W., de Gouw, J., Jimenez, J. L., and Wang, J.: Droplet activation properties of organic aerosols observed at an urban site during CalNex-LA, Journal of Geophysical Research-Atmospheres, 118, 2903–2917, https://doi.org/10.1002/jgrd.50285, 2013.

Metcalf, A. R., Craven, J. S., Ensberg, J. J., Brioude, J., Angevine, W., Sorooshian, A., Duong, H. T., Jonsson, H. H., Flagan, R. C., and Seinfeld, J. H.: Black carbon aerosol over the Los Angeles Basin during CalNex, Journal of Geophysical Research: Atmospheres, 117, https://doi.org/10.1029/2011JD017255, 2012.

Middlebrook, A. M., Bahreini, R., Jimenez, J. L., and Canagaratna, M. R.: Evaluation of Composition-Dependent Collection Efficiencies for the Aerodyne Aerosol Mass Spectrometer using Field Data, Aerosol Science and Technology, 46, 258–271, https://doi.org/10.1080/02786826.2011.620041, 2012.

Moffet, R. C., O'Brien, R. E., Alpert, P. A., Kelly, S. T., Pham, D. Q., Gilles, M. K., Knopf, D. A., and Laskin, A.: Morphology and mixing of black carbon particles collected in central California during the CARES field study, Atmos. Chem. Phys., 16, 14515–14525, https://doi.org/10.5194/acp-16-14515-2016, 2016.

Mohr, C., Huffman, J. A., Cubison, M. J., Aiken, A. C., Docherty, K. S., Kimmel, J. R., Ulbrich, I. M., Hannigan, M., and Jimenez, J. L.: Characterization of Primary Organic Aerosol Emissions from

Meat Cooking, Trash Burning, and Motor Vehicles with High-Resolution Aerosol Mass Spectrometry and Comparison with Ambient and Chamber Observations, Environ. Sci. Technol., 43, 2443–2449, https://doi.org/10.1021/es8011518, 2009.

Moteki, N. and Kondo, Y.: Effects of Mixing State on Black Carbon Measurements by Laser-Induced Incandescence, Aerosol Science and Technology, 41, 398–417, https://doi.org/10.1080/02786820701199728, 2007.

Nordmann, S., Cheng, Y. F., Carmichael, G. R., Yu, M., Denier van der Gon, H. A. C., Zhang, Q., Saide, P. E., Pöschl, U., Su, H., Birmili, W., and Wiedensohler, A.: Atmospheric black carbon and warming effects influenced by the source and absorption enhancement in central Europe, Atmos. Chem. Phys., 14, 12683–12699, https://doi.org/10.5194/acp-14-12683-2014, 2014.

Paatero, P. and Tapper, U.: Positive matrix factorization: A non-negative factor model with optimal utilization of error estimates of data values, Environmetrics, 5, 111–126, https://doi.org/10.1002/env.3170050203, 1994.

Peng, J., Hu, M., Guo, S., Du, Z., Zheng, J., Shang, D., Levy Zamora, M., Zeng, L., Shao, M., Wu, Y.-S., Zheng, J., Wang, Y., Glen, C. R., Collins, D. R., Molina, M. J., and Zhang, R.: Markedly enhanced absorption and direct radiative forcing of black carbon under polluted urban environments, Proceedings of the National Academy of Sciences, 113, 4266–4271, https://doi.org/10.1073/pnas.1602310113, 2016.

Philippin, S., Wiedensohler, A., and Stratmann, F.: Measurements of non-volatile fractions of pollution aerosols with an eight-tube volatility tandem differential mobility analyzer (VTDMA-8), Journal of Aerosol Science, 35, 185–203, https://doi.org/10.1016/j.jaerosci.2003.07.004, 2004.

Ren, J., Zhang, F., Wang, Y., Collins, D., Fan, X., Jin, X., Xu, W., Sun, Y., Cribb, M., and Li, Z.: Using different assumptions of aerosol mixing state and chemical composition to predict CCN concentrations based on field measurements in urban Beijing, Atmospheric Chemistry and Physics, 18, 6907–6921, https://doi.org/10.5194/acp-18-6907-2018, 2018.

Riemer, N., Ault, A. P., West, M., Craig, R. L., and Curtis, J. H.: Aerosol Mixing State: Measurements, Modeling, and Impacts, Reviews of Geophysics, 57, 187–249, https://doi.org/10.1029/2018RG000615, 2019.

Roberts, G. C. and Nenes, A.: A continuous-flow streamwise thermal-gradient CCN chamber for atmospheric measurements, Aerosol science and technology, 39, 206–221, 2005.

Rose, D., Gunthe, S. S., Mikhailov, E., Frank, G. P., Dusek, U., Andreae, M. O., and Pöschl, U.: Calibration and measurement uncertainties of a continuous-flow cloud condensation nuclei counter (DMT-CCNC): CCN activation of ammonium sulfate and sodium chloride aerosol particles in theory and experiment, Atmos. Chem. Phys., 8, 1153–1179, 2008.

Rose, D., Nowak, A., Achtert, P., Wiedensohler, A., Hu, M., Shao, M., Zhang, Y., Andreae, M. O., and Poschl, U.: Cloud condensation nuclei in polluted air and biomass burning smoke near the mega-city Guangzhou, China - Part 1: Size-resolved measurements and implications for the modeling of aerosol particle hygroscopicity and CCN activity, Atmos. Chem. Phys., 10, 3365–3383, 2010.

Rose, D., Gunthe, S. S., Su, H., Garland, R. M., Yang, H., Berghof, M., Cheng, Y. F., Wehner, B., Achtert, P., Nowak, A., Wiedensohler, A., Takegawa, N., Kondo, Y., Hu, M., Zhang, Y., Andreae,

M. O., and Poschl, U.: Cloud condensation nuclei in polluted air and biomass burning smoke near the mega-city Guangzhou, China -Part 2: Size-resolved aerosol chemical composition, diurnal cycles, and externally mixed weakly CCN-active soot particles, Atmos. Chem. Phys., 11, 2817–2836, https://doi.org/10.5194/acp-11-2817-2011, 2011.

Saha, P. K., Khlystov, A., and Grieshop, A. P.: Downwind evolution of the volatility and mixing state of near-road aerosols near a US interstate highway, Atmos. Chem. Phys., 18, 2139–2154, https://doi.org/10.5194/acp-18-2139-2018, 2018.

Sedlacek, A. J., Lewis, E. R., Kleinman, L., Xu, J., and Zhang, Q.: Determination of and evidence for non-core-shell structure of particles containing black carbon using the Single-Particle Soot Photometer (SP2), Geophysical Research Letters, 39, L06802, https://doi.org/10.1029/2012GL050905, 2012.

Shi, J., Hong, J., Ma, N., Luo, Q., He, Y., Xu, H., Tan, H., Wang, Q., Tao, J., Zhou, Y., Han, S., Peng, L., Xie, L., Zhou, G., Xu, W., Sun, Y., Cheng, Y., and Su, H.: Measurement report: On the difference in aerosol hygroscopicity between high and low relative humidity conditions in the North China Plain, Atmos. Chem. Phys., 22, 4599–4613, https://doi.org/10.5194/acp-22-4599-2022, 2022.

Stevens, R., Ryjkov, A., Majdzadeh, M., and Dastoor, A.: An improved representation of aerosol mixing state for air quality–weather interactions, Atmos. Chem. Phys., 22, 13527–13549, https://doi.org/10.5194/acp-22-13527-2022, 2022.

Stolzenburg, M. R. and McMurry, P. H.: Equations governing single and tandem DMA configurations and a new lognormal approximation to the transfer function, Aerosol Science and Technology, 42, 421–432, 2008.

Su, H., Rose, D., Cheng, Y. F., Gunthe, S. S., Massling, A., Stock, M., Wiedensohler, A., Andreae, M. O., and Poschl, U.: Hygroscopicity distribution concept for measurement data analysis and modeling of aerosol particle mixing state with regard to hygroscopic growth and CCN activation, Atmos. Chem. Phys., 10, 7489–7503, https://doi.org/10.5194/acp-10-7489-2010, 2010.

Subramanian, R., Kok, G. L., Baumgardner, D., Clarke, A., Shinozuka, Y., Campos, T. L., Heizer, C. G., Stephens, B. B., de Foy, B., Voss, P. B., and Zaveri, R. A.: Black carbon over Mexico: the effect of atmospheric transport on mixing state, mass absorption cross-section, and BC/CO ratios, Atmos. Chem. Phys., 10, 219–237, https://doi.org/10.5194/acp-10-219-2010, 2010.

Tan, H., Xu, H., Wan, Q., Li, F., Deng, X., Chan, P. W., Xia, D., and Yin, Y.: Design and Application of an Unattended Multifunctional H-TDMA System, Journal of Atmospheric and Oceanic Technology, 30, 1136–1148, https://doi.org/10.1175/JTECH-D-12-00129.1, 2013.

Tao, J., Zhao, C., Nan, M., and Ye, K.: Consistency and applicability of parameterization schemes for the size-resolved aerosol activation ratio based on field measurements in the North China Plain, Atmospheric Environment, 173, 316–324, 2018.

Tao, J., Kuang, Y., Ma, N., Zheng, Y., Wiedensohler, A., and Zhao, C.: An improved parameterization scheme for size-resolved particle activation ratio and its application on comparison study of particle hygroscopicity measurements between HTDMA and DMA-CCNC, Atmospheric Environment, 226, 117403, https://doi.org/10.1016/j.atmosenv.2020.117403, 2020.

Tao, J., Kuang, Y., Ma, N., Hong, J., Sun, Y., Xu, W., Zhang, Y., He, Y., Luo, Q., Xie, L., Su, H., and Cheng, Y.: Secondary aerosol formation alters CCN activity in the North China Plain, Atmos. Chem. Phys., 21, 7409–7427, https://doi.org/10.5194/acp-21-7409-2021, 2021.

Tao, M., Chen, L., Su, L., and Tao, J.: Satellite observation of regional haze pollution over the North China Plain, Journal of Geophysical Research: Atmospheres, 117, https://doi.org/10.1029/2012JD017915, 2012.

Thalman, R., de Sa, S. S., Palm, B. B., Barbosa, H. M. J., Poehlker, M. L., Alexander, M. L., Brito, J., Carbone, S., Castillo, P., Day, D. A., Kuang, C., Manzi, A., Ng, N. L., Sedlacek, A. J., Souza, R., Springston, S., Watson, T., Poehlker, C., Poeschl, U., Andreae, M. O., Artaxo, P., Jimenez, J. L., Martin, S. T., and Wang, J.: CCN activity and organic hygroscopicity of aerosols downwind of an urban region in central Amazonia: seasonal and diel variations and impact of anthropogenic emissions, Atmospheric Chemistry and Physics, 17, 11779–11801, https://doi.org/10.5194/acp-17-11779-2017, 2017.

Ting, Y., Mitchell, E. J. S., Allan, J. D., Liu, D., Spracklen, D. V., Williams, A., Jones, J. M., Lea-Langton, A. R., McFiggans, G., and Coe, H.: Mixing State of Carbonaceous Aerosols of Primary Emissions from "Improved" African Cookstoves, Environ. Sci. Technol., 52, 10134–10143, https://doi.org/10.1021/acs.est.8b00456, 2018.

Tomlin, J. M., Jankowski, K. A., Veghte, D. P., China, S., Wang, P., Fraund, M., Weis, J., Zheng, G., Wang, Y., Rivera-Adorno, F., Raveh-Rubin, S., Knopf, D. A., Wang, J., Gilles, M. K., Moffet, R. C., and Laskin, A.: Impact of dry intrusion events on the composition and mixing state of particles during the winter Aerosol and Cloud Experiment in the Eastern North Atlantic (ACE-ENA), Atmos. Chem. Phys., 21, 18123–18146, https://doi.org/10.5194/acp-21-18123-2021, 2021.

Ulbrich, I. M., Canagaratna, M. R., Zhang, Q., Worsnop, D. R., and Jimenez, J. L.: Interpretation of organic components from Positive Matrix Factorization of aerosol mass spectrometric data, Atmos. Chem. Phys., 9, 2891–2918, https://doi.org/10.5194/acp-9-2891-2009, 2009.

Wang, X., Ye, X., Chen, J., Wang, X., Yang, X., Fu, T.-M., Zhu, L., and Liu, C.: Direct links between hygroscopicity and mixing state of ambient aerosols: estimating particle hygroscopicity from their single-particle mass spectra, Atmos. Chem. Phys., 20, 6273–6290, https://doi.org/10.5194/acp-20-6273-2020, 2020.

Wang, Y., Wang, X., Kondo, Y., Kajino, M., Munger, J. W., and Hao, J.: Black carbon and its correlation with trace gases at a rural site in Beijing: Top-down constraints from ambient measurements on bottom-up emissions, Journal of Geophysical Research: Atmospheres, 116, https://doi.org/10.1029/2011JD016575, 2011.

Wang, Y., Zhang, F., Li, Z., Tan, H., Xu, H., Ren, J., Zhao, J., Du, W., and Sun, Y.: Enhanced hydrophobicity and volatility of submicron aerosols under severe emission control conditions in Beijing, Atmos. Chem. Phys., 17, 5239–5251, https://doi.org/10.5194/acp-17-5239-2017, 2017.

Wang, Y., Hu, R., Wang, Q., Li, Z., Cribb, M., Sun, Y., Song, X., Shang, Y., Wu, Y., Huang, X., and Wang, Y.: Different effects of anthropogenic emissions and aging processes on the mixing state of soot particles in the nucleation and accumulation modes, Atmos. Chem. Phys., 22, 14133–14146, https://doi.org/10.5194/acp-22-14133-2022, 2022.

Wehner, B., Berghof, M., Cheng, Y. F., Achtert, P., Birmili, W., Nowak, A., Wiedensohler, A., Garland, R. M., Pöschl, U., Hu, M., and Zhu, T.: Mixing state of nonvolatile aerosol particle fractions and comparison with light absorption in the polluted Beijing region, Journal of Geophysical Research: Atmospheres, 114, https://doi.org/10.1029/2008JD010923, 2009.

Wu, Y., Wang, X., Tao, J., Huang, R., Tian, P., Cao, J., Zhang, L., Ho, K.-F., Han, Z., and Zhang, R.: Size distribution and source of black carbon aerosol in urban Beijing during winter haze episodes, Atmos. Chem. Phys., 17, 7965–7975, https://doi.org/10.5194/acp-17-7965-2017, 2017.

Xu, W., Sun, Y., Wang, Q., Zhao, J., Wang, J., Ge, X., Xie, C., Zhou, W., Du, W., Li, J., Fu, P., Wang, Z., Worsnop, D. R., and Coe, H.: Changes in Aerosol Chemistry From 2014 to 2016 in Winter in Beijing: Insights From High-Resolution Aerosol Mass Spectrometry, Journal of Geophysical Research: Atmospheres, 124, 1132–1147, https://doi.org/10.1029/2018JD029245, 2019.

Xu, W. Y., Zhao, C. S., Ran, L., Deng, Z. Z., Liu, P. F., Ma, N., Lin, W. L., Xu, X. B., Yan, P., He, X., Yu, J., Liang, W. D., and Chen, L. L.: Characteristics of pollutants and their correlation to meteorological conditions at a suburban site in the North China Plain, Atmos. Chem. Phys., 11, 4353–4369, https://doi.org/10.5194/acp-11-4353-2011, 2011.

Yang, Z., Ma, N., Wang, Q., Li, G., Pan, X., Dong, W., Zhu, S., Zhang, S., Gao, W., He, Y., Xie, L., Zhang, Y., Kuhn, U., Xu, W., Kuang, Y., Tao, J., Hong, J., Zhou, G., Sun, Y., Su, H., and Cheng, Y.: Characteristics and source apportionment of black carbon aerosol in the North China Plain, Atmospheric Research, 276, 106246, https://doi.org/10.1016/j.atmosres.2022.106246, 2022.

Zhang, F., Li, Y., Li, Z., Sun, L., Li, R., Zhao, C., Wang, P., Sun, Y., Liu, X., Li, J., Li, P., Ren, G., and Fan, T.: Aerosol hygroscopicity and cloud condensation nuclei activity during the AC3Exp campaign: implications for cloud condensation nuclei parameterization, Atmos. Chem. Phys., 14, 13423–13437, https://doi.org/10.5194/acp-14-13423-2014, 2014.

Zhang, S., Shen, X., Sun, J., Zhang, Y., Zhang, X., Xia, C., Hu, X., Zhong, J., Wang, J., and Liu, S.: Atmospheric Particle Hygroscopicity and the Influence by Oxidation State of Organic Aerosols in Urban Beijing, Journal of Environmental Sciences, 124, 544–556, https://doi.org/10.1016/j.jes.2021.11.019, 2023.

Zhang, S. L., Ma, N., Kecorius, S., Wang, P. C., Hu, M., Wang, Z. B., Größ, J., Wu, Z. J., and Wiedensohler, A.: Mixing state of atmospheric particles over the North China Plain, Atmospheric Environment, 125, 152–164, 2016.

Zhang, Y., Su, H., Ma, N., Li, G., Kecorius, S., Wang, Z., Hu, M., Zhu, T., He, K., Wiedensohler, A., Zhang, Q., and Cheng, Y.: Sizing of Ambient Particles From a Single-Particle Soot Photometer Measurement to Retrieve Mixing State of Black Carbon at a Regional Site of the North China Plain, Journal of Geophysical Research: Atmospheres, 123, 12,778-12,795, https://doi.org/10.1029/2018JD028810, 2018.

Zhao, G., Tao, J., Kuang, Y., Shen, C., Yu, Y., and Zhao, C.: Role of black carbon mass size distribution in the direct aerosol radiative forcing, Atmos. Chem. Phys., 19, 13175–13188, https://doi.org/10.5194/acp-19-13175-2019, 2019.

Zhao, G., Tan, T., Hu, S., Du, Z., Shang, D., Wu, Z., Guo, S., Zheng, J., Zhu, W., Li, M., Zeng, L., and Hu, M.: Mixing state of black carbon at different atmospheres in north and southwest China, Atmos. Chem. Phys., 22, 10861–10873, https://doi.org/10.5194/acp-22-10861-2022, 2022.

Zheng, H., Kong, S., Wu, F., Cheng, Y., Niu, Z., Zheng, S., Yang, G., Yao, L., Yan, Q., Wu, J., Zheng, M., Chen, N., Xu, K., Yan, Y., Liu, D., Zhao, D., Zhao, T., Bai, Y., Li, S., and Qi, S.: Intra-regional transport of black carbon between the south edge of the North China Plain and central China during winter haze episodes, Atmos. Chem. Phys., 19, 4499–4516, https://doi.org/10.5194/acp-19-4499-2019, 2019.

Zhuang, B. L., Li, S., Wang, T. J., Deng, J. J., Xie, M., Yin, C. Q., and Zhu, J. L.: Direct radiative forcing and climate effects of anthropogenic aerosols with different mixing states over China, Atmospheric Environment, 79, 349–361, https://doi.org/10.1016/j.atmosenv.2013.07.004, 2013.